Summer 6-15-2021

Cross-Junction Based Metasurfaces: A Roadmap to Fano Resonances

Mirna Soliman
mirnahafez@aucegypt.edu

The American University in Cairo

Department of Electronics and Communications Engineering

« Cross-Junction Based Metasurfaces: A Roadmap to Fano Resonances »

By

Mirna Magdy ElSayed Hafez Mohamed Soliman

A thesis submitted to the Department of Electronics and Communications Engineering
in conformity with the requirements
for the degree of
Master of Science
at The American University in Cairo
May 2021

« Cross-Junction Based Metasurfaces: A Roadmap to Fano Resonances»

« Electronics and Communication Engineering Department »
The American University in Cairo
«18^{th} May 2021 »

Abstract

The first part of the thesis presents a summary of the classification of materials, followed by the development of metamaterials and their salient role. Then, a study of metamaterials and the evolution of these 3D structures to 2D, known as metasurfaces, have been discussed. Moreover, the physics and practical interest behind Fano resonance have been discussed. Furthermore, the physical fundamentals guiding the performance of both the metamaterials and metasurfaces, including the temporal coupled-mode theory and the generalized laws of reflection and refraction, have been intensely investigated, along with some of the outstanding properties of the metamaterials. Then, a comparison between metamaterials and photonic/electronic bandgap materials, in addition to a comparison between metasurfaces and frequency-selective surfaces, has been shown. Finally, a literature review for previous work on the application of metasurfaces in different fields and the progress of Fano resonance in numerous applications are stated.

The second part of the thesis presents the research work that has been done, in which a design for an electromagnetic metasurface in the microwave regime has been proposed. Breaking the structural symmetry of the unit cell constituting the metasurface is shown to introduce a route for inducing high-quality factor (Q) Fano resonance (FR). The total thickness of the structure is deeply subwavelength, with the metasurface's thickness equal to 0.08 of the wavelength. The design has been fabricated and characterized inside an anechoic chamber. Both numerical and measured data show to be in perfect agreement. This work paves the way for numerous applications, including but not limited to sensing and polarization rotation.

Thesis Advisor: Professor Yehea Ismail
Title: Professor, Fellow IEEE
Director of the Center of Nanoelectronics and Devices (CND), Zewail City of Science and Technology, The American University in Cairo
Distinguished Lecturer of IEEE CASS

Thesis Co-Advisor: Dr. Ahmed M. Mahmoud
Title: Assistant Professor

Acknowledgments

I want to express my sincere gratitude to my thesis advisors, Professor Yehea Ismail, who did not hesitate to supervise and support me during a very tough time, and Dr. Ahmed M. Mahmoud, who has invested his total effort during the pandemic in guiding me to achieving the goal. Thank you is not enough for your continuous support, patience, and encouragement, which always helped me to stay on task and schedule. I feel fortunate to work under the supervision of highly outstanding professors in their fields.

I also want to express a Special appreciation to the Microwave Lab in Faculty of Engineering, Ain Shams University and its director, Dr. Amr Safwat, and his STDF project group for giving me access to use computational simulation (CST Studio) and measuring facilities (Antenna Room and Network Analyzer) in his lab and their support during the measurement and their stimulating ideas and remarks that helped me during my research work.

Table of Contents

Table of Contents

List of Figures

List of Tables

Chapter 1

1. Introduction

Metamaterials are very intriguing human-made materials that are used in various applications due to their unique electromagnetic properties. In this chapter, a brief overview of the conventional electromagnetic materials is mentioned, and the purpose of this novel, human-made materials that surpass traditional materials, is deeply investigated. Furthermore, such distinctive behavior has been enhanced by developing these 3D materials into 2D, called metasurfaces. Finally, some brief introductory notes on Fano resonance are mentioned.

1.1 History of Materials

The material properties involved in any system mainly describe its response to the existence of electromagnetic waves. The two main properties that merely describe this electromagnetic performance are the permeability and the permittivity of these materials. A very common classification for the electromagnetic behavior of materials is based on the sign of the permeability and permittivity, as shown in Figure 1. Any dielectric material has a positive permeability and permittivity and they exist in nature abundantly. Dielectric materials fall into a category called “Double-Positive Medium or forward-wave propagation medium,”. That is the regular medium that is well studied such as silicon, air and water. When a wave is incident on a surface, part of it is reflected, and another is transmitted in a forward direction.

The second classification is called epsilon-negative medium, which exists when we have a negative permittivity and a positive permeability. A good example for that is the noble metals (silver, gold) and plasmas. These materials are not rare. Also, if silicon is doped properly, it can have a negative epsilon in the mid infrared range.

The third classification is the gyroptropic materials. In this case, the permittivity is positive, while the permeability is negative. This classification is referred to as a “Mu-negative medium,”. Gyrotropic materials can be referred to as magneto-optic materials or ferrites.

The last classification is to have both negative permeability and negative permittivity at the same frequency. These Double negative materials, to the best of our knowledge, are not found in nature. It is believed that these materials were the origin of the metamaterials field. Veselago was the first scientist who initiated this work in 1967. He studied theoretically the behavior of light on having a DNG material. The metamaterial domain started where researchers were trying to realize a behavior similar to that of the DNG using the common known materials [1], [2].

Those materials' performance can be understood by implementing several models, such as the Lorentz model, Debye model, and Drude model [1].

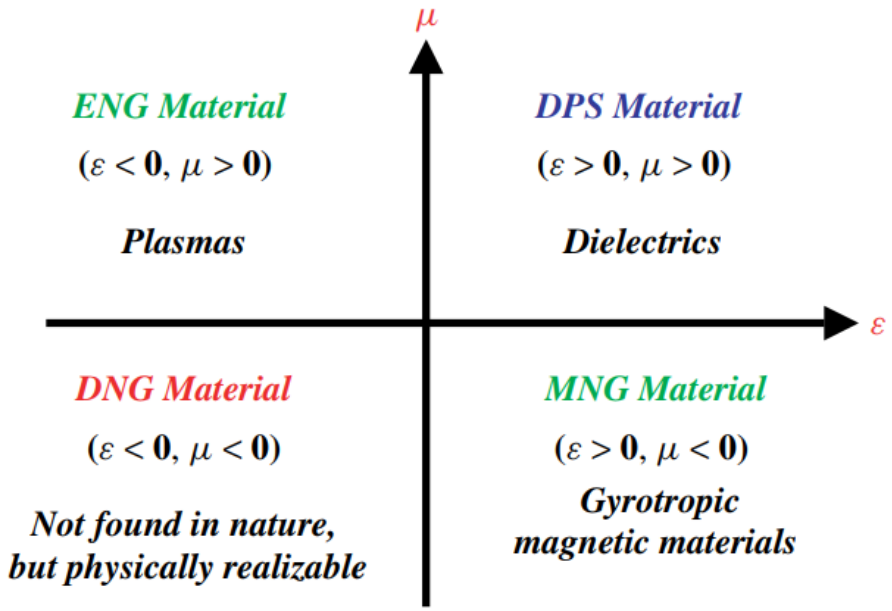

Figure 1: Classification of Materials [1]

1.2 The need for Metamaterials

Despite the several definitions in literature that have arisen for the word "metamaterials," they all agree on the fact that metamaterials have had an influx of interest in recent years which can be ascribed to their ability to exhibit interesting electromagnetic and optical properties unattainable previously by using naturally existing materials and distinguished from the properties of its constituents [1], [3].

Accordingly, having the ability to employ and engineer wave properties permits a new era of innovative applications in microwave and optical regimes. Furthermore, Metamaterials enable substantial miniaturization in the components' size, along with improvement in their performance [1].

It is worth mentioning that the remarkable properties of a metamaterial usually emerge because of its geometrical structure. Hence, the geometrical properties of the metamaterials, such as size, density, composition, and arrangement, play a vital role in tailoring the metamaterials' behavior [1].

1.3 Important Metamaterials' structures

The late nineteenth century (1898) witnessed the emerging of metamaterials for electromagnetic applications in the microwave regime by Jagadis Chunder Bose, who worked on elements with chiral properties [1]. Followed by Lindman [4] in 1914, who studied the electromagnetism of chiral media. That paved the way during the twentieth century to explore several applications for metamaterials and their exotic behavior, including negative refraction angles, near-zero index, and negative refractive index, which the commonly known materials cannot achieve. In literature, materials with negative refractive index, as shown in Figure *2*, are referred to as Left-handed Metamaterials [2], double-negative (DNG) materials [1], or Veselago medium, owing to the scientist who initiated this work in 1967 [3], [5]. They possess negative effective permittivity and negative effective permeability at the same frequency and result in wave propagation in a backward manner. [2], [3]. Such behavior occurs due to the opposite flow direction between the phase and the group velocity. The concept of backward waves was even brought up in the early twentieth century (1904) by Lamb [6], who studied mechanical systems and observed the existence of such waves. As for the materials with near-zero index, the real part of either the permittivity or the permeability is meant to be approximately zero [7]. Recently, these artificial materials and their outstanding performance have led off numerous research activities and the emerging of innovative microwave and optical applications, [1] including beamformers [8] as shown in Figure *3*, cavity resonators [5], and absorbers [9].

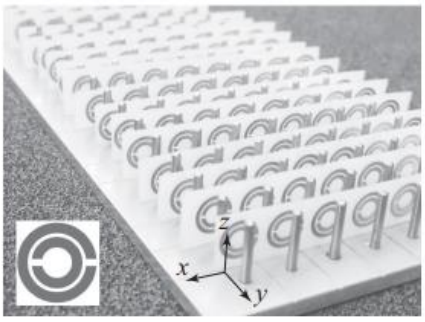

Figure 2: Double-negative Materials, consisting of thin wires and split rings resonators [2]

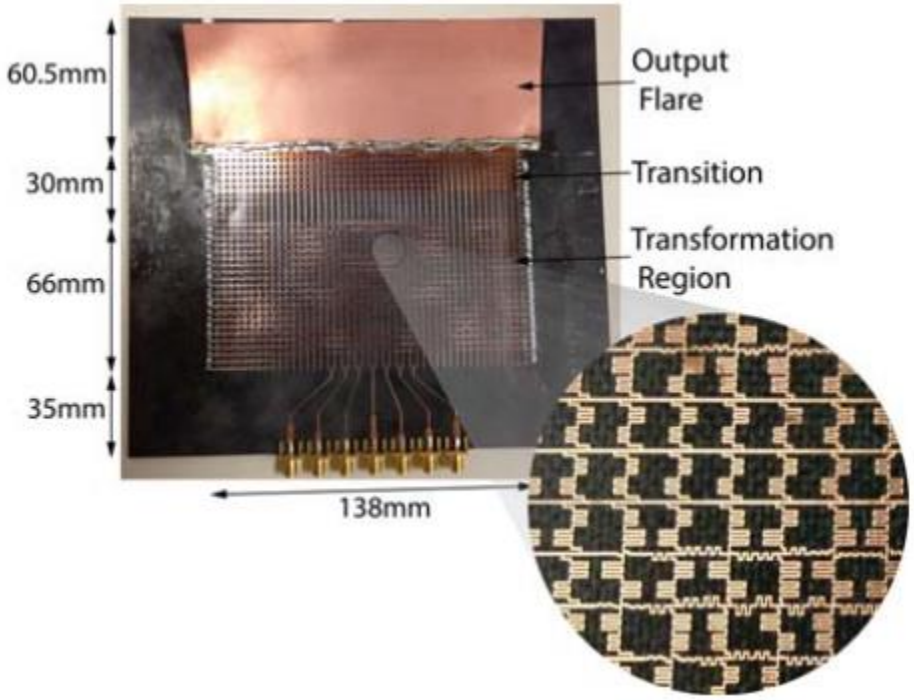

Figure 3: Fabricated PCB beamformer [8]

1.4 Metasurfaces

By year 2000, metamaterials were 3D bulk structures that suffered from losses. Their size was large, so their integration with technology was not very smooth. Accordingly, metamaterials did not lead off in industry until the introduction of metasurfaces.

Metasurfaces are a two-dimensional (2D) or quasi 2D extension of metamaterials [10]–[12]. Their structures are lateral or transverse in plane. Their thickness is as small as possible and they manipulate the wave in 2D, rather than 3D. Metasurfaces have introduced a new class of metamaterials that, in addition to generally leading to less stringent loss constraints, they are also easier to fabricate and hence attain a wider range of applications in practical systems and applications. In literature, metasurfaces can be referred to as meta-films or single-layer metamaterials [7]. Metasurfaces can be used to manipulate the radiation patterns of antennas [8], reconfigurable and tunable devices [13], controllable surfaces [7] and holograms [14], as illustrated in Figure *4*. Due to the highly resonant behavior of the metasurfaces, they exhibit high sensing capabilities. Additionally, it was proven that utilizing metasurfaces overcomes the limitations on classical resonators' dimensions [5], [15].

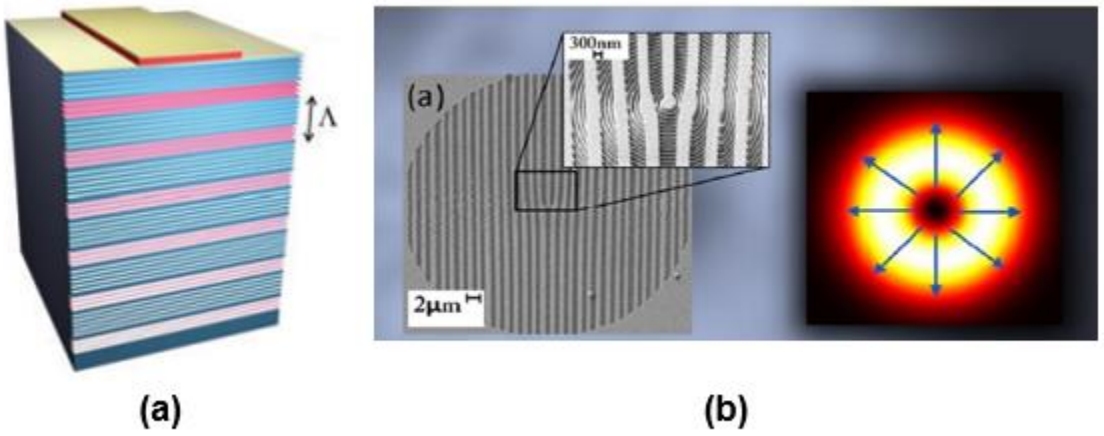

Figure 4: (a) Metasurface structures used in beam engineering *[16]* (b) Metasurface structures used in designing holograms *[14]*

1.5 Fano resonance (FR)

From the various applications of metasurfaces, this thesis focuses on working on a certain application, which is the Fano resonance. The FR is a resonance characterized by a unique, asymmetric profile compared to the conventional evenly shaped resonance profiles. Fano resonant response has been observed during the past decade in plasmonic metasurfaces, nanoparticles, and electromagnetic metamaterials. Its spectral response plays a vital role in

various applications, such as biological and chemical sensing, cloaking[17]–[19], and modulators [20], as demonstrated in Figure 5.

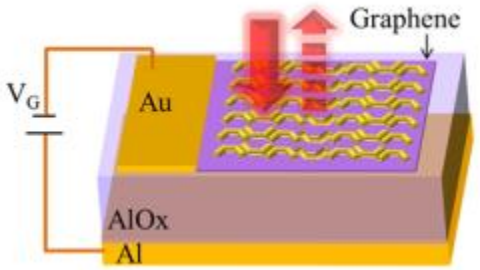

Figure 5: Optical Modulator formed of electrically tunable absorber operating in the mid-infrared range *[20]*

Chapter 2

2. Physical Fundamentals and Technical Background

In this chapter, the physical fundamentals and background governing the unprecedented performance of metamaterials and metasurfaces are investigated. Then, a comparison between metamaterials and photonic/electronic bandgap materials, in addition to a comparison between metasurfaces and frequency-selective surfaces, will be shown. Besides, the technical background guiding the concept of Fano resonance is shown.

Fano resonance first emerged in physics by the physicist Ugo Fano while he was theoretically explaining the peculiar line shape generated as an outcome of the inelastic scattering of electrons from helium [21]. Accordingly, his analysis was more related to physical concepts and terms that are too complex and hard to be utilized systematically. So, in this section, the analysis is studied from an engineering point of view to facilitate its understanding.

2.1 Metamaterials and Metasurfaces

Metamaterials exhibit unique electric and magnetic properties that make them a good candidate in several applications, like, biosensors, broadband light manipulation, and energy harvesting.

2.1.1 Double Negative Material

As mentioned before, the behavior of any material on an applied electromagnetic field is attributed to its relative permittivity (ε_r) and permeability (μ_r) (relative to the vacuum permittivity and permeability parameters, $\epsilon_{r,vacuum} = \mu_{r,vacuum} = 1$) of this material. Dielectrics, for example, have positive relative permittivity and permeability, other materials behave differently, but our focus here is on the double negative behavior. There is no material found in nature in this intriguing region that exhibits a double negative behavior (both relative permittivity and permeability are negative). Fortunately, we can engineer and design these materials. Moreover, some materials have different electromagnetic parameters on various frequencies, which means these parameters do not have a constant value. They are dependent on

the frequency. So, our goal here is to model the electric properties as a function of the frequency of these double negative materials [1].

Let us focus on the electric properties of a material under an applied electric field. At the equilibrium state, nothing happens, and the material is not polarized. A polarization from an atomic point of view is the displacement of an electron cloud far from the nucleus generating a dipole between it and the positively charged nucleus. The Lorentz model is a mathematical model used to model the electric properties of materials based on the assumption that the electrons are moving due to the applied electric field with a damped factor. We want to model the electric susceptibility χ_e, where $\varepsilon_r = 1 + \chi_e$ and P_i is the polarization density due to an applied electric field.

$$\frac{d^2}{dt^2}P_i(\omega) + \frac{\Gamma_L d}{dt}P_i + \omega_0^2 P_i = \epsilon_0 \chi_L E_i \qquad (1)$$

where the first term is the accelerating term, the second term is the damping term, the third term is the restoring force term, and the free term is the driving force due to the electric field E_i

The solution of the equation (1) is written as,

$$P_i(\omega) = \frac{\epsilon_0 \chi_L E_i}{-\omega^2 + j\Gamma_L \omega + \omega_0^2} \qquad (2)$$

$$\chi_{e,Lorentz}(\omega) = \frac{P_i(\omega)}{\epsilon_0 E_i} = \frac{\chi_L}{-\omega^2 + j\Gamma_L \omega + \omega_0^2} \qquad (3)$$

From this model, there are exceptional cases,

1st case – the acceleration term is small relative to the other terms:

$$\chi_{e,Debye}(\omega) = \frac{P_i(\omega)}{\epsilon_0 E_i} = \frac{\chi_d}{j\Gamma_d \omega + \omega_0^2} \qquad (4)$$

2nd case – the restoring force is small relative to the other terms:

The physical meaning of small restoring force is that the electrons are not bound.

$$\chi_{e,Drude}(\omega) = \frac{P_i(\omega)}{\epsilon_0 E_i} = \frac{\chi_D}{-\omega^2 + j\Gamma_L \omega} \qquad (5)$$

The only two cases that can yield a negative susceptibility are Lorentz and Drude model as the Lorentz model exhibits a resonance over a narrow range, while the Drude model can exhibit

negative electric susceptibility over a larger range, governed by the following inequality $\omega^2 < \chi_D - \Gamma_L^2$. A lossy Drude model is widely used in modeling metamaterials [1].

For magnetic susceptibility (χ_m), the same analysis with H_i as the driving force and M_i as the magnetic response could be used, resulting in the same expression.

2.1.2 Scattering in Metamaterials

When an electromagnetic wave is incident on a material, part of the electric field is reflected, and the other part is transmitted, as demonstrated in Figure *6*. The ratio between the reflected and incident wave and the transmission and incident wave are reflection and transmission coefficients receptively [1].

$$R = \frac{\eta_2 - \eta_1}{\eta_2 + \eta_1} * \frac{1 - e^{-j2k_2 d}}{1 - \left[\frac{(\eta_2 - \eta_1)}{(\eta_2 + \eta_1)}\right]^2 e^{-j2k_2 d}} \qquad (6)$$

$$T = \frac{4\eta_2 \eta_1}{(\eta_2 + \eta_1)^2} * \frac{e^{-jk_2 d}}{1 - \left[\frac{(\eta_2 - \eta_1)}{(\eta_2 + \eta_1)}\right]^2 e^{-j2k_2 d}} \qquad (7)$$

where $k_i = \omega\sqrt{\varepsilon_i}\sqrt{\mu_i}$ and $\eta_i = \sqrt{\mu_i}/\sqrt{\varepsilon_i}$

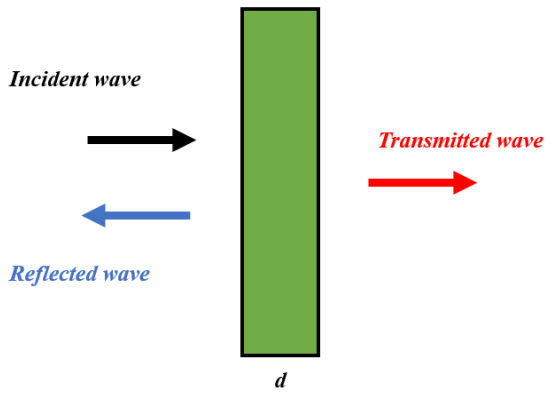

Figure 6: Schematic scattering of an incident wave on a material.

Assume a matched double-negative (DNG) material that means $\eta_1 = \eta_2$, $R = 0$ and $T = e^{jk_2 d}$

It is evident that the transmitted wave in DNG material will add a positive phase shift, unlike the conventional double-positive (DPS) material that adds a negative phase shift. From this point, we can conclude that metamaterials that exhibit DNG behavior could be used in phase compensation applications [1].

2.1.3 Generalized Laws of Reflection and Refraction

Beam formation can be manipulated with the commonly known optical devices depending on the gradual phase shift gathered along the wave path. When an electromagnetic wave is incident on the interface of two media with different refractive indices, part of the incident wave is reflected in the first medium. The other part is transmitted to the second medium. Such behavior and the beam direction are guided by the continuity equation governing the electromagnetic waves at the boundary and by the optical characteristics of the two media separated at the interface. This is shown in Fresnel equations and Snell's law, respectively. In classical optics, it is generally presumed that the interface between any two media is ideal, introducing no change to the light beam falling on it. However, the introduction of metasurfaces introduces new degrees of freedom and a difference in the boundary conditions. They give rise to new terms in the laws of reflection and refraction by applying Fermat's principle [11], [12], [22].

Arranging the unit cells of metasurfaces in a particular fashion allows complete control over the wavefront, phase, polarization, and the properties of light. When the light collides at the interface of metasurfaces, each unit cell introduces a distinct phase shift, different from the neighboring one. On collision, a surface plasmon phenomenon occurs, where a surface electromagnetic wave is induced, oscillating the charges found in the unit cell. This surface wave and the fundamental incident wave interact, resulting in the phase discontinuity across the metasurface, as shown in Figure *7*; thus, replacing the commonly used Snell's law with a generalized law of refraction [22] and replacing the conventional law of reflection with a generalized law of reflection [23].

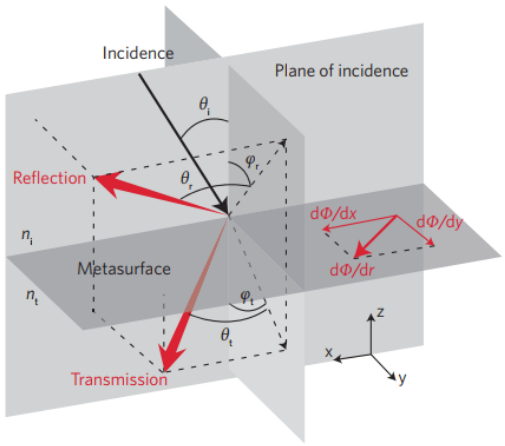

Figure 7: Phase Shift exists along the metasurface interface resulting in random reflection and refraction directions *[23]*

To be able to understand how the electromagnetic wave acts on interaction with a metasurface, it is essential to derive the generalized laws of reflection and refraction.

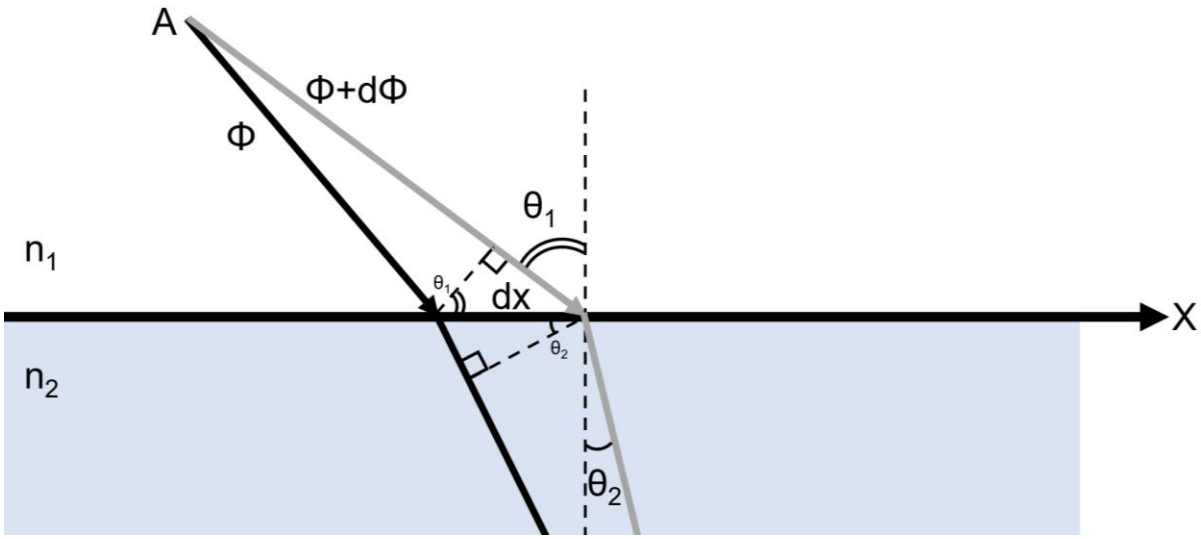

Figure 8: Sketch illustrating the derivation of the generalized law of refraction on having a wave incident at the interface, tailored with metasurfaces between two media with different refractive indices.

In Figure *8*, let us presume that the two optical paths are significantly close to the real light path, then the total phase difference between the two paths is zero. [12] The total phase of the grey path can be written as the summation of its path difference and its phase ($\Phi + d\Phi$). The path difference of the grey path can be written as

$$\Delta Path_1 = sin(\theta_1)dx \qquad (8)$$

$$Phase_1 = \left(\frac{2\pi}{\lambda_1}\right) * \Delta Path_1 + (\Phi + d\Phi) \qquad (9)$$

While the phase of the black path can be written as the summation of its path difference and its phase (Φ). The path difference of the black path can be written as

$$\Delta Path_2 = sin(\theta_2)dx \qquad (10)$$

$$Phase_2 = \left(\frac{2\pi}{\lambda_2}\right) * \Delta Path_2 + \Phi \qquad (11)$$

where θ_1 and θ_2 are the angle of incidence and refraction, respectively, and λ_1 and λ_2 are the effective wavelength of the first and second medium, respectively. The total phase difference between the two lines can be written as,

$$k_0\, n_1\, sin(\theta_1)dx + (\Phi + d\Phi) - k_0\, n_2\, sin(\theta_2)dx - \Phi = 0 \qquad (12)$$

where $k_0 = \frac{2\pi}{\lambda_0}$, where λ_0 is the free space wavelength.

By some algebraic manipulations, we get

$$k_0\, n_1 sin(\theta_1)dx + (d\Phi) - k_0\, n_2\, sin(\theta_2)dx = 0 \qquad (13)$$

$$n_2\, sin(\theta_2) - n_1\, sin(\theta_1) = \frac{1}{k_0}\frac{d\phi}{dx} \qquad (14)$$

Upon investigating the generalized Snell's law of refraction, which is illustrated in equation (14), it can be noticed that the light beam could be refracted in a random direction, given that a convenient steady phase gradient exists along the interface. And from this nonzero phase gradient, we can deduce that different refractive angles would be obtained from the two incident angles ($\pm\theta_i$). Thus, such salient behavior allows tailoring the wavefronts and accordingly paved the way for various applications, including beam steering [24], beam focusing [22], and polarization change [22].

If no phase shift exists parallel or perpendicular to the plane of incidence, equation (14) would be expressed as shown in equation (15), which is the conventionally known Snell's law governing the refraction of light propagating along plane surfaces.

$$n_t\, sin(\theta_t) = n_i\, sin(\theta_i) \qquad (15)$$

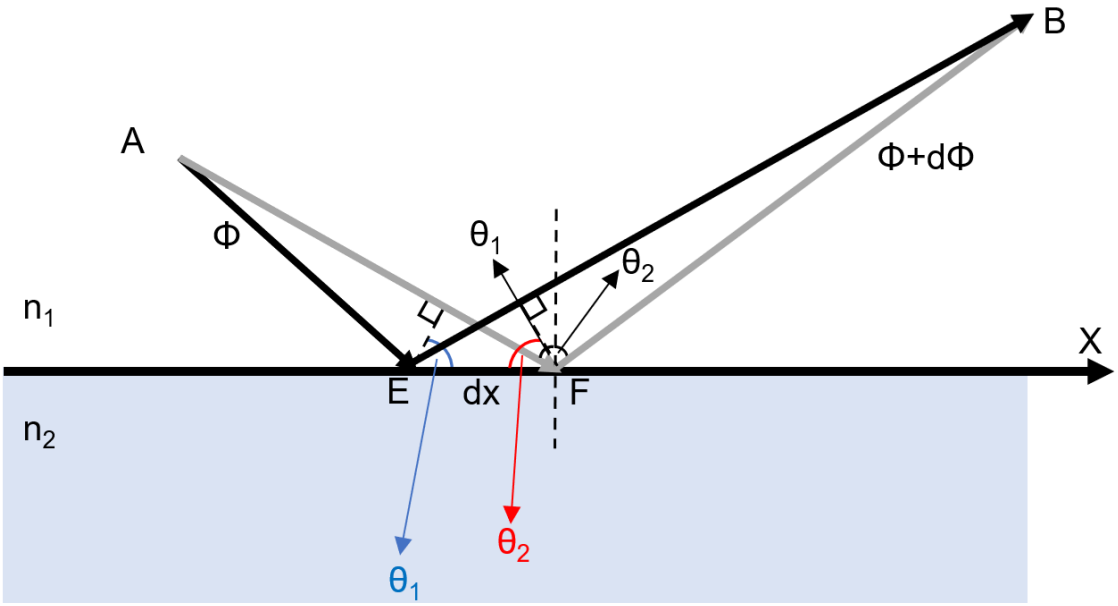

Figure 9: Sketch illustrating the derivation of the generalized law of reflection on having a wave incident at the interface, tailored with metasurfaces between two media with different refractive indices.

Similarly, in Figure *9*, let us presume that the two optical paths (AEB and AFB) are significantly close to the real light path passing from point A to B, then the total phase difference between the two paths is zero [25]. The total phase of the grey path is due to the path difference and its phase ($\Phi + d\Phi$), the path difference of the grey path will be written as

$$\Delta Path_1 = sin(\theta_1)dx \qquad (16)$$

$$Phase_1 = \left(\frac{2\pi}{\lambda_1}\right) * \Delta Path_1 + (\Phi + d\Phi) \qquad (17)$$

While the phase of the black path is due to the path difference and its phase (Φ), the path difference of the black path will be written as

$$\Delta Path_2 = sin(\theta_2)dx \qquad (18)$$

$$Phase_2 = \left(\frac{2\pi}{\lambda_1}\right) * \Delta Path_2 + \Phi \qquad (19)$$

where θ_1 and θ_2 are the angle of incidence and reflection, respectively, and λ_1 is the effective wavelength of the first medium. The total phase difference between the two lines will be written as,

$$k_0\, n_1\, sin(\theta_1)dx + (\Phi + d\Phi) - k_0\, n_1\, sin(\theta_2)dx - \Phi = 0 \qquad (20)$$

where $k_0 = \frac{2\pi}{\lambda_0}$, where λ_0 is the free space wavelength.

By some algebraic manipulations, we get

$$k_0\, n_1 sin(\theta_1)dx + (d\Phi) - k_0\, n_1\, sin(\theta_2)dx = 0 \qquad (21)$$

$$sin(\theta_2) - sin(\theta_1) = \frac{1}{n_1 k_0}\frac{d\phi}{dx} \qquad (22)$$

Thus, the generalized law of reflection, demonstrated in equation (22), indicates that the light beam could be reflected in a random direction, based on the refractive indices of the surrounding media and the phase gradient existing at the interface.

In case no phase gradient occurs along the interface, then equation (22) could be simplified to the conventional equation governing reflection on plane surfaces, which states that the angle of reflection must be equal to the angle of incidence, as shown in equation (23)

$$\theta_1 = \theta_2 \qquad (23)$$

Furthermore, it was commonly known that there is only one critical angle found when light passes from a denser medium to a lower dense one with a transmission angle equals to 90°. When the incident angle is greater than this critical angle, total internal reflection takes place. However, when the light falls on a metasurface, there would be two critical angles.

From equation (14), by setting $\theta_2 = 90°$ and solving for θ_1, we get that the critical angle is as follows, taking into consideration the different refractive angle obtained by each of θ_1 and $-\theta_1$ as a result of the non-zero phase gradient.

$$\theta_c = sin^{-1}(\pm\frac{n_2}{n_1} - \frac{1}{k_0 n_1}\frac{d\phi}{dx}) \qquad (24)$$

2.2 Metamaterials compared to photonic bandgap (PBG) or electromagnetic bandgap (EBG) structure

Metamaterials are three-dimensional (3D) artificial structures of metal and dielectric. They are usually constructed out of arrays of scatterers [7], [9] that exhibit strong interactions with the incident electromagnetic fields due to the resonant features of the constituent unit cells [7].

To understand the difference between metamaterials and bandgap structures, it is worth spotlighting the classification of periodic composite materials and their electromagnetic behavior based on the operating wavelength scale, as shown in Figure *10*. When the wavelength of the propagating wave is large compared to the dimensions of the unit cell, the structure can be studied using the classical effective medium method [7]. When the wavelength becomes comparable to the dimensions of the unit cell, the structure exhibits resonances due to both the individual resonances of the unit cells and the periodicity of the structure. Metamaterials emerge when the resonance is due to the individual resonances of the unit cells. However, when the lattice of the structure resonates, this gives rise to photonic bandgap (PBG) or electromagnetic bandgap (EBG) material. These materials are characterized by the existence of passbands, at which the electromagnetic waves are permitted to flow, and stopbands, at which EM waves are blocked.

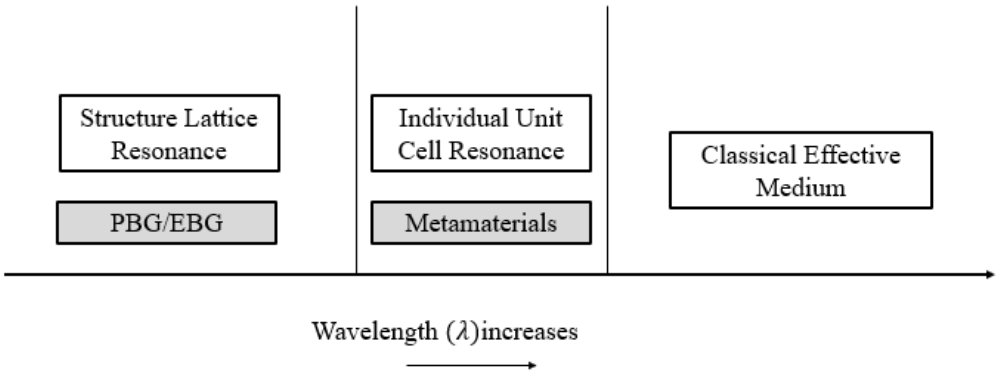

Figure 10: 3D Composite material classification regions

2.3 Metasurfaces compared to frequency-selective surfaces

The same approach mentioned with metamaterials in section 2.2 is applicable with metasurfaces, as demonstrated in Figure *11*. Metasurfaces emerge when the resonance is due to the individual resonances of the unit cells. However, when the lattice of the structure resonates, this gives rise to frequency-selective surfaces [7]. Frequency selective surfaces are established from repeatedly arranged units, which are fabricated of metal with random geometries with the aim of absorbing or reflecting electromagnetic waves based on the operating frequency, thus

behaving as a filter [26] in the communication field. Each unit of these FSS resonant at the frequency of resonance, and they are separated with a distance equal to half the wavelength of the aforementioned frequency. There are other applications in which frequency selective surfaces are implemented. Other than being used in signal filtering, they could be used as beam splitters and some antenna components fabrication [27].

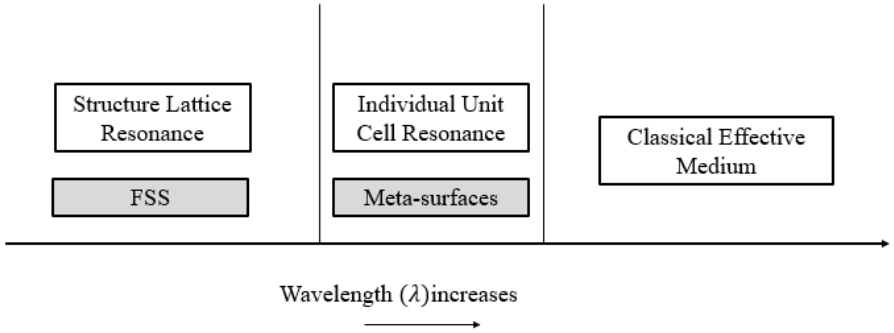

Figure 11: 2D Composite material classification regions

2.4 Temporal Coupled-Mode Theory

The temporal coupled-mode theory is used to describe the dynamical behavior of mode coupling in a time-dependent formalism. If we have two modes, *B* and *D*, as shown in Figure 12, at small proximity of each other and one of them is excited, then this mode will be coupled to the other mode [28]. Assume the excited mode will be in the form of

$$B = be^{j\omega_b t} \qquad (25)$$

The derivative respect to the time will be written as

$$\frac{dB}{dt} = j\omega_b B \qquad (26)$$

where, $|B|^2$ is the energy stored in the mode and ω_b is the frequency of the excited mode.

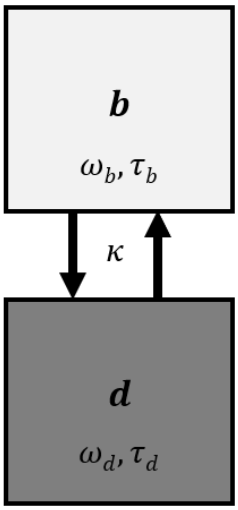

Figure 12: A schematic of two modes coupling with each other, while the first mode is excited due to an incident wave.

Equation (26) assumes that the mode does not radiate energy. If we presume radiative losses, then the equation will be,

$$\frac{dB}{dt} = j\omega_b B - \tau_b^{-1} B \qquad (27)$$

where, τ_b is the radiative lifetime.

At equilibrium, after adding the coupling coefficient, the two systems equation of the two modes can be written in this form,

$$\frac{dB}{dt} = -j\omega_b B + \tau_b^{-1} B + j\kappa D = 0 \qquad (28)$$

$$\frac{dD}{dt} - j\omega_d D + \tau_d^{-1} D + j\kappa B = 0 \qquad (29)$$

2.5 Resonance

The term “resonance” refers to a sharp peak or dip in the field spectral response when the frequency of the incident electromagnetic wave is close to or equal to the natural frequency of the designed structure. Such behavior can be made use of in numerous applications, such as biosensing and resonators.

2.6 Fano Resonance

The term “Fano Resonance (FR)” was used to describe the asymmetrical spectral lines of the energetic atoms from a quantum mechanics point of view. The mechanism of Fano resonance resembles the mechanism of Auger recombination as explained below. To be more specific, assume we have an energetic photon that bombards an atom or a molecule. This energetic photon will excite an electron from its bound state. The mechanism of excitation has two different paths,

1- An electron gained enough energy, which makes it transit from a bound state to an unbound state.
2- A mechanism like Auger recombination (it is a type of recombination between electron/hole pairs, where, an excess amount of energy is transferred to another electron during recombination), where an electron got excited and transferred its energy to another electron, the second electron got ionized from the atom to an unbound state, while the original electron is relaxed to its original state.

The second mechanism is the one that we want to focus on because a resonance arises from it due to electron-electron excitation and interaction. The asymmetric pattern of spectral lines is a result of the quantum-mechanical interaction between the two different paths. So, FR is, briefly, a quantum-mechanical interaction of energetic electron-electron interaction forming constructive or destructive interferences.

In photonics, FR is a little bit different. Since there is no electrons excitation in photonics, Fano resonance is an interaction between two electromagnetic modes in the metamaterial. These two resonance modes got excited by an incident electromagnetic field resembling a high-energetic photon. The reflected wave will be a constructive or instructive interference of these two modes, depending on their lifetimes, wavelengths, and dipole strength. The two modes are called “bright” and “dark,” the bright mode is characterized by strong incident electromagnetic wave coupling and a shorter radiative lifetime. In comparison, the dark mode is characterized by weak incident electromagnetic wave coupling and longer radiative lifetime [29].

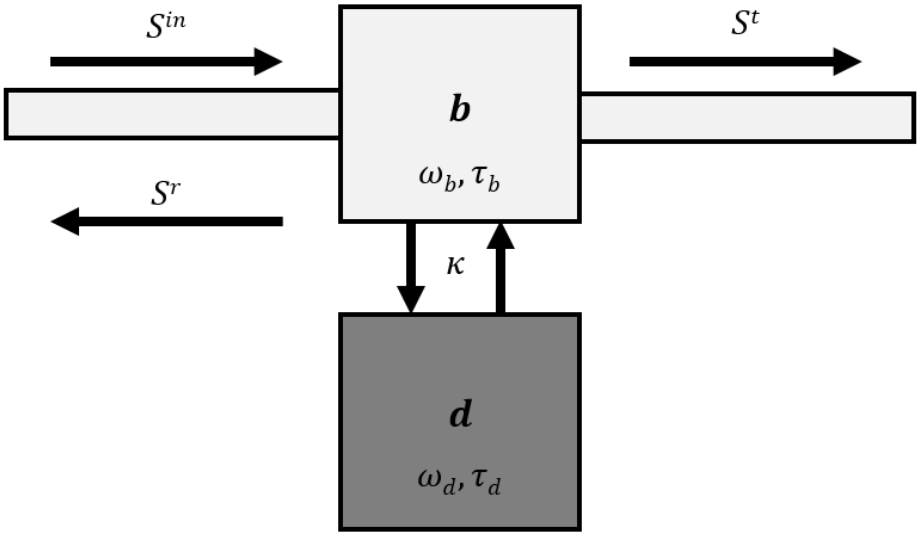

Figure 13: A schematic of two resonators coupling with each other, while the first resonator is excited due to an incident wave.

If we assumed that the meta-molecule is modeled as single input/output port coupling resonators, as shown in Figure 13, we can employ the equations governing the coupling between the incident wave with the bright resonator and the two resonators coupling with each other are as following,

$$\dot{b} - j\left(\omega_b + \frac{j}{\tau_b}\right) b + j\kappa d = \alpha_b S^{in} e^{j\omega t} \qquad (30)$$

$$\dot{d} - j\left(\omega_d + \frac{j}{\tau_d}\right) d + j\kappa b = 0 \qquad (31)$$

where, b and d are the amplitudes of the bright and dark modes receptively, S^{in} is the amplitude of the incident wave with natural frequency ω, τ is the radiative lifetime that models the radiative losses, α_b is the coupling factor between the incident wave the bright mode, and κ is the coupling factor between the bright and the dark modes within the two resonators. The free term in equation (30) is due to the incident wave exciting the bright mode in the first resonator.

The reflection and transmission coefficient of the incident wave is given by,

$$r = \frac{S^r}{S^{in}} = \frac{-|\alpha_b|^2 j\left(\omega - \omega_d - \frac{j}{\tau_d}\right)}{\left(\omega - \omega_b - \frac{j}{\tau_b}\right)\left(\omega - \omega_d - \frac{j}{\tau_d}\right) - \kappa^2} \qquad (32)$$

$$t = \frac{S^t}{S^{in}} = 1 + r \qquad (33)$$

where, the reflected and transmitted wave are given by $S^r = \alpha_b^* b$ and $S^t = S^{in} + S^r = S^{in} + \alpha_b^* b$ in terms of the amplitude of the bright mode.

To generalize equation (32), we can include non-radiative losses as another lifetime τ^0, where the reciprocal of the total lifetime will be the summation of the reciprocal of the individual lifetimes (Radiative and non-radiative lifetimes), its equation is given by this formula,

$$\frac{1}{\tau_{b,d}} = \frac{1}{\tau_{b,d}^0} + \frac{1}{\tau_{b,d}^R} \qquad (34)$$

Now, let us calculate the decay of the stored energy in the two resonators assuming the incident wave amplitude is zero $S^{in} = 0$ and the medium is lossless to have a relation between the radiative lifetime of the bright mode and the coupling coefficient between the bright mode and the incident wave. By assuming an infinite lifetime for the dark mode ($\tau_d = \infty$), and the coupling coefficient is zero ($\kappa = 0$), the total decay of the stored energy will be solely due to the bright mode's stored energy decay,

$$\frac{d}{dt}W = \frac{d}{dt}(|b|^2 + |d|^2) = -\frac{2|b|^2}{\tau_b} - \frac{2|d|^2}{\tau_d} = -\frac{2|b|^2}{\tau_b} \qquad (35)$$

By imposing the conservation of energy condition $\left(1 = |r|^2 + |t|^2 \rightarrow \left|S^{in}\right|^2 = |S^r|^2 + |S^t|^2\right)$, the decay of the stored energy can be,

$$\frac{d}{dt}W = -\frac{2|b|^2}{\tau_b} = |S^r|^2 + |S^t|^2 = -2|\alpha_b|^2|b|^2 \qquad (36)$$

From equations (35) and (36), we can notice that the coupling coefficient of the incident wave with the bright mode is related to the bright mode lifetime by this equation, $\frac{1}{\tau_b} = |\alpha_b|^2$.

This model can easily predict the spectral response of a system before running any simulations. It also verifies the physical analogy that was explained for the coupling between the two modes. The next step is to determine the reflectance and transmittance at a given input angular frequency.

Assuming lossless environment ($\frac{1}{\tau^0} = 0$), so by plotting the reflectance and transmittance using equation (32), with different δ, where $\delta = \omega_b - \omega_d$, three curves are plotted for each of them with different δ ($\delta = 0.1\omega_b, 0\ and\ -0.1\omega_b$) and the Fano resonance of each curve will be

investigated. The different lifetimes and the coupling coefficient used to plot the reflectance and transmittance are illustrated in Table *1*.

Table 1: Parameters used to generate the reflectance and transmittance graphs.

Description	Parameter	Value
Bright mode radiative lifetime	τ_b^R	$\frac{10}{\omega_b}$
Dark mode radiative lifetime	τ_d^R	∞
Non-radiative lifetime (Ohmic)	τ^0	∞
Coupling Coefficient	κ	$0.05\ \omega_b$

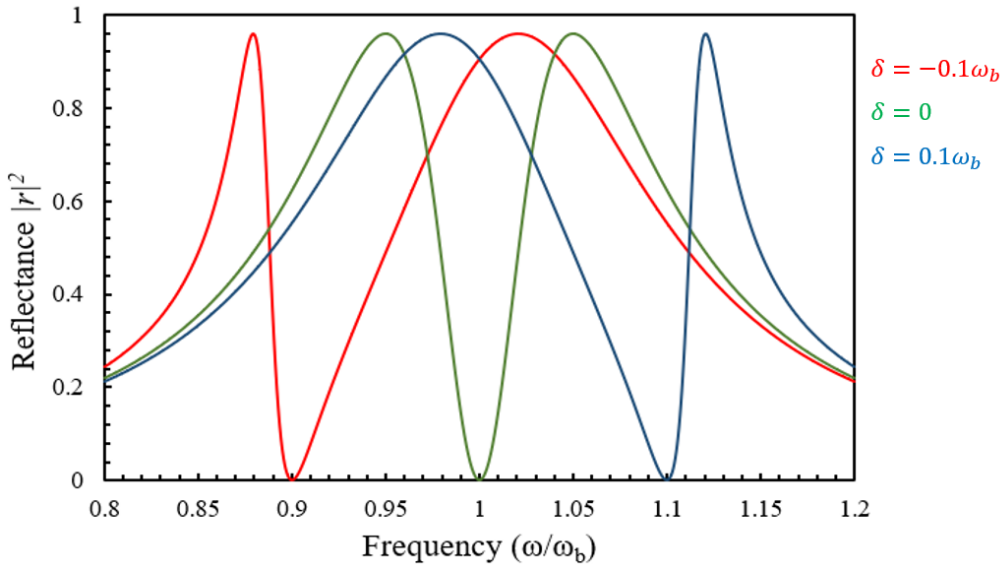

Figure 14: A graph of reflectance assuming negligible Ohmic losses. The red and blue curves correspond to the Fano resonance's asymmetric behavior, while the green figure is the electromagnetically induced transparency case.

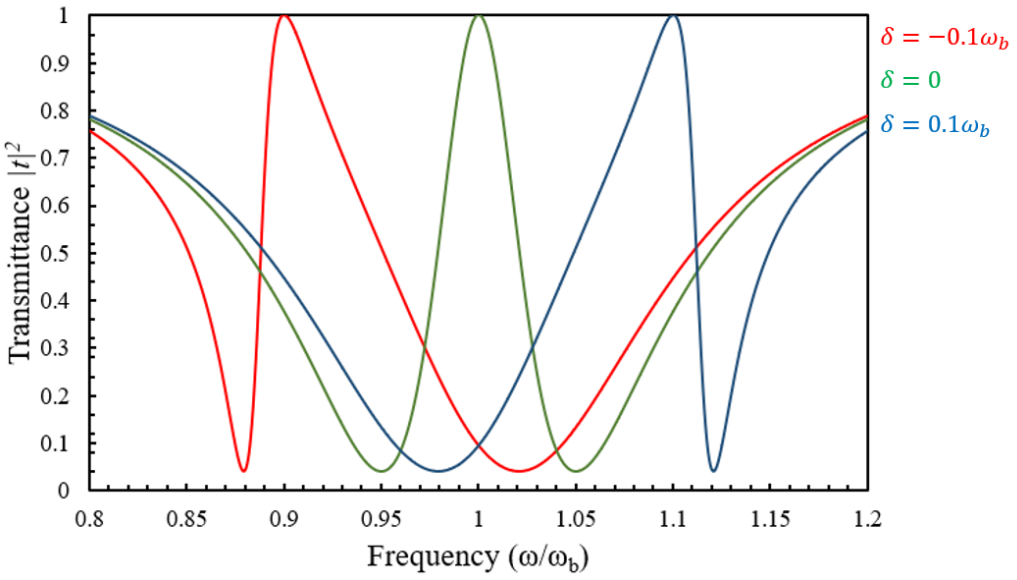

Figure 15: The transmittance of the three Fano resonance cases. It is noticeable that by adding both curves (Reflectance and Transmittance), the value will be one (Ohmic losses are negligible)

In Figure *14* at $\omega = \omega_b$, it is evident that the reflection peaks of both the red and blue curves have a relatively broad range, however, at $\omega = \omega_d$, the reflection exhibits a sharp dip. Due to the interface between the two modes, the asymmetric behavior of the reflectance and the transmittance is noticeable at $\omega_b \neq \omega_d$ as shown in Figure *14* and Figure *15*. By adding non-radiative losses ($\frac{1}{\tau^0}$ is finite), the magnitude of the reflectance will be reduced.

A particular case is evident in Figure *14* and Figure *15*, where $\delta = 0$, this is known as electromagnetically induced transparency (EIT). This is a special case of FR at which the bright and dark modes occur at the same frequency. It needs complex unit cells to design it. In the literature, some designs are implementing this concept by using metamaterial's structure.

Chapter 3

3. Literature Review and Previous Work

In this chapter, a literature review for the applications of metasurfaces in the different fields is presented. In addition, research work that has been done on Fano resonance with various efficiency and applications is stated.

3.1 Applications of Metasurfaces in various regimes

Recently, metasurfaces have been involved in a wide range of microwave applications. Metasurfaces can behave as waveguides, capable of trapping and guiding the electromagnetic wave along a specific path by inserting metasurfaces on both of their sides. These metasurfaces have been designed to cause total reflection of any incident wave falling on it [7], as shown in Figure *16*.

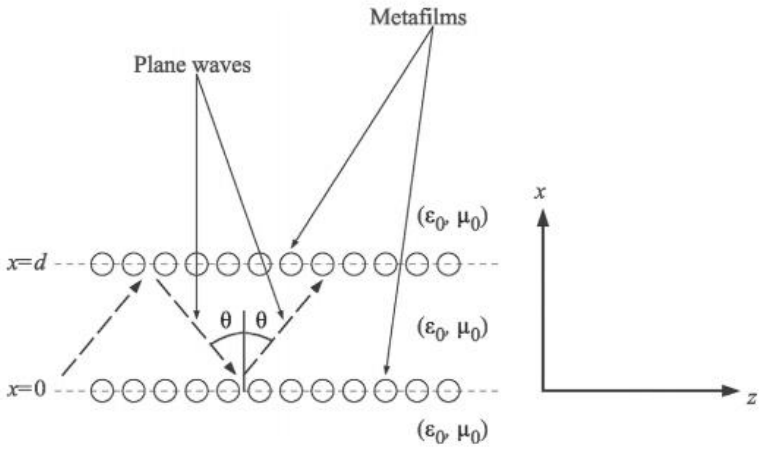

Figure 16:A schematic of waveguide consisting of metasurfaces.[7]

In the late twentieth century, metasurfaces have widely invaded applications in the chemistry domain. Their central role was to enhance the coupling between the analyte and the electromagnetic waves. So, they merely act as chemical and biochemical catalysis [7]. Furthermore, metasurfaces also have a strong influence in the biomedical field. Metasurfaces are used as biosensors capable of measuring the resonant shift due to any change in the refractive index of the surrounding medium.

The main applications that are extensively built on the concept of phase gradient and the introduction of beam shaping are V-shaped metasurfaces with an anisotropic design. Such design grants 360° phase control of any incident wave. However, it suffers from high reflection losses that strongly impact its transmission efficiency to the half [23], [30]. To overcome these reflection losses, Huygens' surfaces have been introduced. In 2013, Pfeiffer et al. [31] manipulated wavefronts in the microwave spectral region using metamaterial Huygens' surfaces, which are referred to as reflectionless surfaces. That work was based on Huygens' principle to gain complete control of wavefronts. Such principle states that every single locus on the wavefront gives rise to new spherical wavelets, which interfere with each other. Pfeiffer designed these reflectionless surfaces by adjusting the metasurface electric (α_e) and magnetic (α_m) polarizabilities to satisfy equation (37), where η_0 represents the surrounding medium impedance.

$$\sqrt{\alpha_e \alpha_m} = \eta_0 \qquad (37)$$

Accordingly, this introduces an alteration in the boundary conditions at the metasurfaces and causes scattering of the wavefronts. Figure *17* shows Pfeiffer's design, which is composed of a pattern of 12-unit cells spread on the substrate. Those patterns are formed of copper designs on one side of a substrate, producing electric polarization currents and split-ring resonators on the other side of producing magnetic polarization currents. Such design achieved 86% transmission efficiency at $10\ GHz$.

(a)

(b)

Figure 17: (a) Huygens' surface with the copper design of 12-unit cells on the top side (b) Huygens' surface with SRR on the bottom side *[31]*

Pfeiffer et al. [32] not only implemented Huygens' surfaces in the microwave field but also introduced them in the optical region to witness their effect in bending the incident light beam efficiently, as illustrated in Figure *18*. He designed an isotropic unit cell fabricated of gold sheets with a certain pattern on a dielectric substrate. The fabrication process took place using electron beam lithography. Such design permits manipulating the wavefronts of the light beam falling onto the metasurface. Furthermore, Pfeiffer introduced a parallel LC circuit model for his design and solved the reflection and transmission properties using the ABCD matrix.

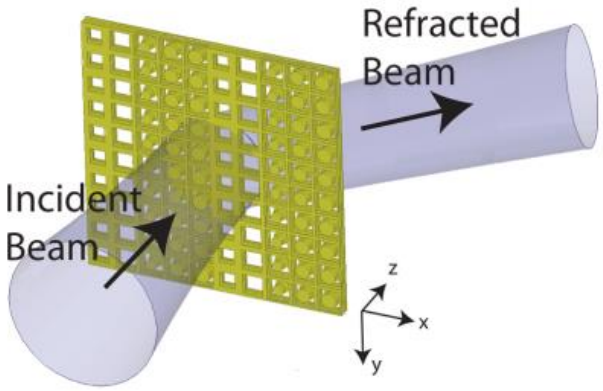

Figure 18:Huygens' surface formed of a periodic array of 5 unit cells in the optical region *[32]*

In 2013, Monticone et al. [30] controlled the transmission of optical nanocircuits through Huygens metasurfaces. He designed cascaded arrays of metal and dielectric of variant ratios, which work as LC nanocircuit components. Such design proved its efficiency to function as a deflector and focusing lens by tailoring the impedance of the surface and varying its materials' ratio.

Furthermore, an ultrathin lens could be designed by metasurfaces. In 2014, Capasso et al. [23] managed to emphasize the progress of metasurface flat, ultrathin components in the optical regime. These components result in phase gradients and instantaneous changes in the light wave amplitude and polarization. He pointed out that to have beam focusing at a certain distance (a), the phase profile of the metasurface should follow equation (38)

$$\phi_L(x,y) = \frac{2\pi}{\lambda}\left(\sqrt{x^2+y^2+a^2}-a\right) \qquad (38)$$

Such profile guarantees an essential condition for focusing, which is converting the shape of the incident wavefront from planar to spherical. When the electromagnetic wave is normally

incident on the surface of a flat lens, the reflected and transmitted wavefronts keep the spherical shape, which results in a high numerical aperture. On the other hand, if the incidence was not normal to the surface, a phenomenon called “coma” occurs, at which a remarkable degradation in the numerical aperture occurs. In this phenomenon, the metasurface exhibits a linear phase profile. Consequently, the transmitted and reflected wavefronts lose their spherical shape, and they no longer follow the phase profile mentioned in equation (38).

Furthermore, metasurfaces were not only used in microwave, optical, and communication regimes, but they also proved their efficiency in the electronics field by protecting sensitive electrical components and minimizing unwanted interference. Such feature was introduced using non-linear metasurfaces, in which diodes and capacitors are included in the structure design and manipulate the metasurface performance by absorbing the RF signals with high power and reducing any external distortion caused to signals with low power.

Based on the superior features owned by metasurfaces and their inclusion in numerous applications, they still face several challenges, such as exhibiting steady spectral response over a wide range of frequency for RF applications, which require wide bandwidth. In addition, further investigation could be done to design switchable and active metasurfaces. This initiative would be easy to fabricate and economical.

3.2 Fano Resonance Applications

By 2007, the term “Fano resonance” has not yet been widely spread or common. It was thought by then that the high-quality factor, which is defined as the ratio between the frequency at which the resonance occurs, and the resonant width as shown in equation (39), was extremely difficult to be achieved in metasurfaces. This restriction to small values was due to the strong coupling of the metasurface unit cells to free space, which leads to high radiation losses. And also, the dimensions of the metasurfaces are known to be in the order of sub-wavelength, which is insufficient to hold and confine the electromagnetic wave [33].

$$Q = \frac{f}{\Delta f} \quad (39)$$

However, in 2002, it was theoretically mentioned that trapped modes could be excited in metasurfaces when the structural symmetry of the metasurface is broken [3]. It is worth noting that the term “trapped modes” is the same as “Fano resonance.” Also, Fano resonance was sometimes referred to as “extraordinary optical transmission (EOT). In 2007, Fedotov managed to observe those sharp resonance on designing an array of asymmetric split rings metasurface structures with an overall size $220\ mm * 220\ mm$. He studied the performance of two different asymmetric structures, the first one denoted with “Type A” with different arc length and the second one denoted with “Type B” with different splits, as shown in Figure *19*.

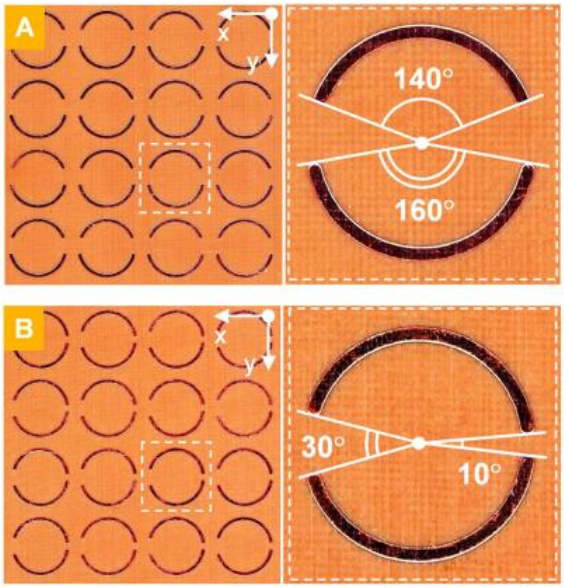

Figure 19: Structure "A" represents a symmetric split ring, while structure "B" represents an asymmetric split ring metasurface structure *[33]*.

He referred the appearance of this Fano resonance to the excitation of symmetric current modes or as called “inaccessible modes” arisen due to weak coupling with free space on breaking the structure symmetry. He also stated the strong correlation between the reflection and transmission structure behavior with the polarization state of the incident wave. The most substantial spectral response was captured on the orthogonality of the electric field to the mirror line of the structures mentioned above, which stands for x-polarization for type (A) and y-polarization for type (B).

As shown in Figure 20(a), type (A) structure demonstrated a Fano resonance at around $6\ GHz$, which is referred to by (II) with quality factor $= 20$, one order of magnitude higher than

any previously mentioned metamaterial structure. In addition, the type (B) system showed a Fano resonance at around $5.5\,GHz$. However, in case of a symmetric split rings, no sharp resonance was noticed at all polarization states, which indicates the unavailability of the trapped modes in such a state.

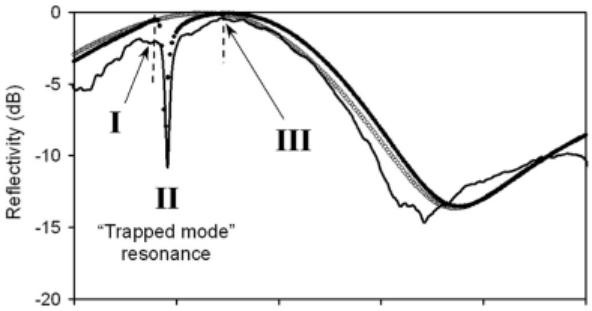

(a)

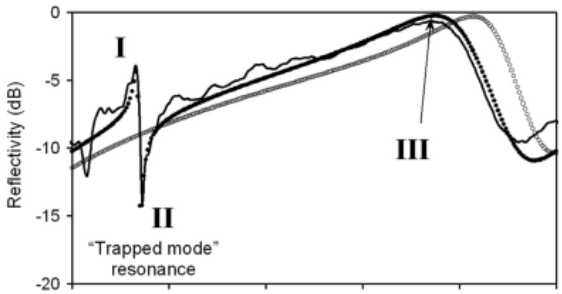

(b)

Figure 20: (a) Reflection spectral response for metasurface structure of Type (A) (b) Reflection spectral response for metasurface structure of Type (B) *[33]*

As illustrated in Figure 21 (a) at region I and III, the currents in both arcs are flowing in the same direction, but with different amplitudes, which are remarkably lower than that in case of region II, leading to the low-quality factor.

However, in Figure 21 (b) at region II, the currents flowing in both arcs of the split ring are opposite in direction but almost equal in magnitude. Thus, resulting in the scattering of weak electromagnetic fields that significantly minimizes the free-space coupling and radiation losses.

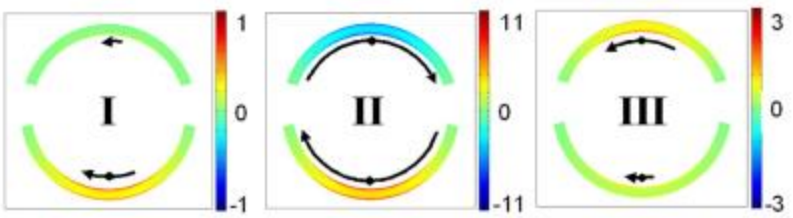

(a)

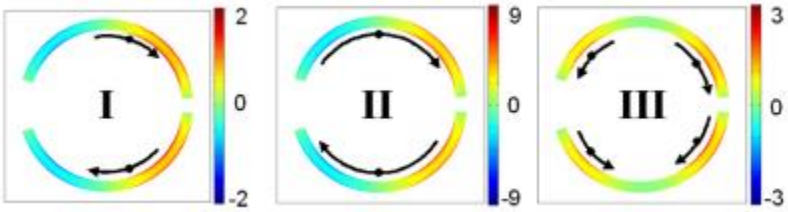

(b)

Figure 21: (a) Current Distribution in Type (A) metasurface (b) Current Distribution in Type (B) metasurface *[33]*

Furthermore, in Figure 22, Fedotov showed that as the asymmetry reduces, the reflection and transmission spectral response would be red-shifted. In addition, on using the lossless dielectric substrate shown in the dashed line graph, a weak relation between the resonant magnitude and the degree of asymmetry exists. Also, the quality factor is inversely proportional to the degree of symmetry. However, on using lossy dielectric as demonstrated in the solid line graph, the same trend is followed until it reaches a summit value and then decreases, which corresponds to higher losses, weaker and broader ‘‘trapped-mode’’ resonance until it vanishes at the symmetric metasurface structure.

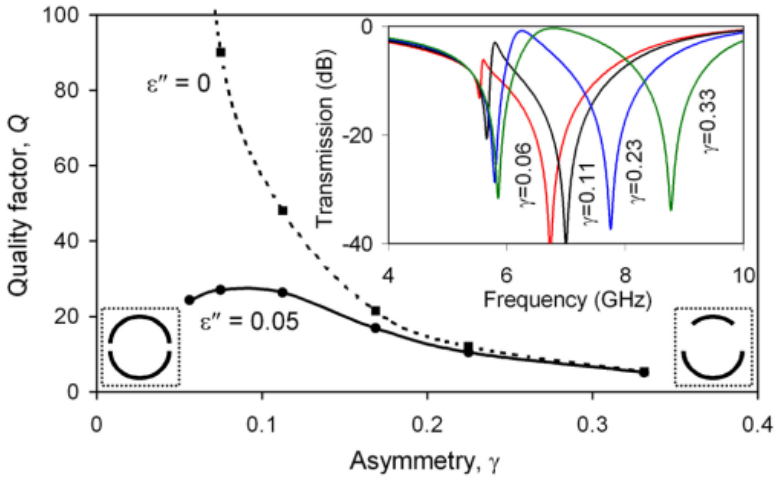

Figure 22: Quality factor of the Fano resonance of Type A structure Vs. asymmetry factor *[33]*

In 2008, Hao et al. [34] and Christ et al. [35] studied the effect of inducing a symmetry break in plasmonic nanocavities, constructed of concentric ring and disk and a structure of two nano-wires gratings separated by a nano-gap respectively, as shown in Figure *23*. Hao stated that both the dipolar disk and ring plasmons interact with each other, giving rise to two types of resonance; bonding resonance which is low in energy, and antibonding one, which is higher in energy. This antibonding resonance is referred to as superradiant as the dipolar disk, and ring plasmons are aligned and in phase, thus resulting in intense radiations. However, the bonding resonance is referred to as sub radiant as the disk and ring plasmons are found to be out of phase. The coupling between both resonances excites the Fano resonance as demonstrated in Figure *24*.

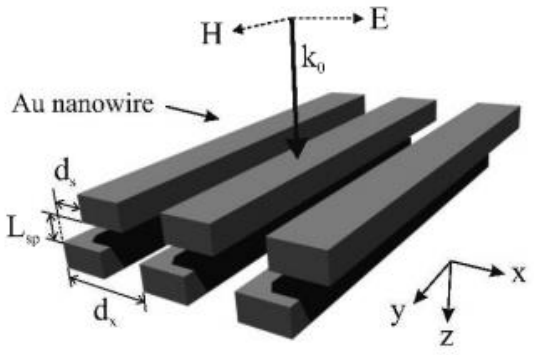

Figure 23: Schematic for the nano gratings proposed by Christ et al. *[35]*

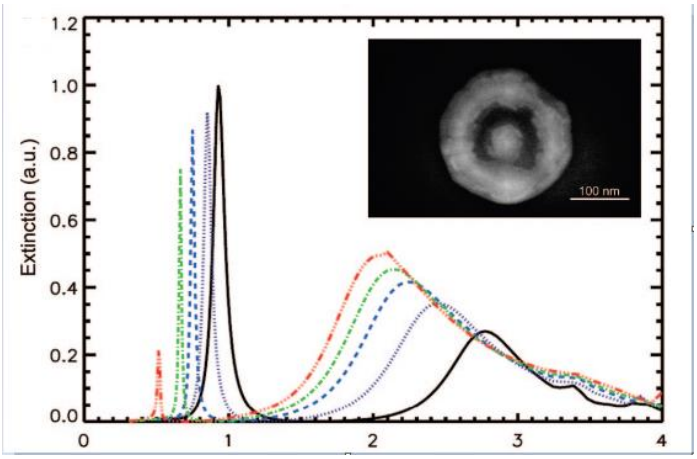

Figure 24:Spectral response showing the Fano resonance along with a parametric sweep of different disk position with respect to the ring *[34]*

In 2013, Pu et al. [36] presented a periodic planar metamaterial formed of 3 repeated metallic wires of different widths in order to break the structure symmetry, thus inducing a sharp Fano resonance. Those wires have a fixed center-to-center distance between adjacent wires and fixed dielectric thickness, as shown in Figure *25*. The electromagnetic wave is incident normally to the surface. [36] used COMSOL Multiphysics to examine the effect of asymmetry introduced in the structure by plotting the transmission spectrum for the symmetric and the asymmetric design as illustrated in Figure *26*. For the asymmetric system, Figure *26* demonstrates a sharp asymmetric peak at 9.8 GH, along with a sharp dip at 10.8 GHz achieving a quality factor of 100.

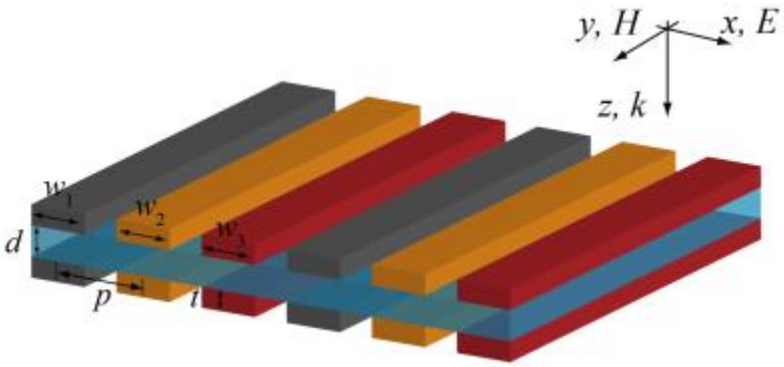

Figure 25:Schematic of a repeated unit cell formed of 3 metallic wires of different widths *[36]*

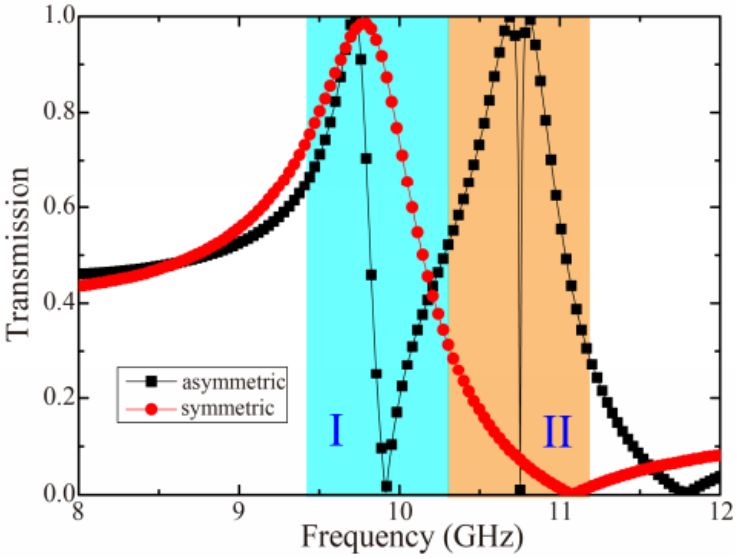

Figure 26: Transmission spectrum for symmetric and asymmetric structures *[36]*

Fano resonance could be physically interpreted in metamaterials by the classical analogy [37], which is a broad, but not thorough definition. It could also be explained by ab initio theory in plasmonic nanostructures and metamaterials depending on the Feshbach formalism [38]. However, it is vague and too complex to be understood. On the other hand, Pu [36] managed to analyze the physical interpretation of Fano resonance using the generalized sheet impedance theory and an appropriate circuit model, by which the effective electric and magnetic impedances can be solved based on the extracted s-parameters from either the simulation or the measurement.

In Figure *26*, it is evident that the symmetric structure exhibits an asymmetric Fano resonance. The notion behind this asymmetric behavior is the interference between the electric and magnetic resonances. This idea is illustrated in Figure *27* by using equation (40) for the sheet impedances. The real and imaginary parts of both electric admittance and magnetic impedance are plotted versus frequency. It is noted that electric admittance has a nearly flat response, while magnetic impedance has just a single narrow resonance.

$$Y_e = 2Y_0 \frac{1 - r - t}{1 + r + t}$$
$$Z_m = 2Z_0 \frac{1 + r - t}{1 - r + t} \quad (40)$$

[32]

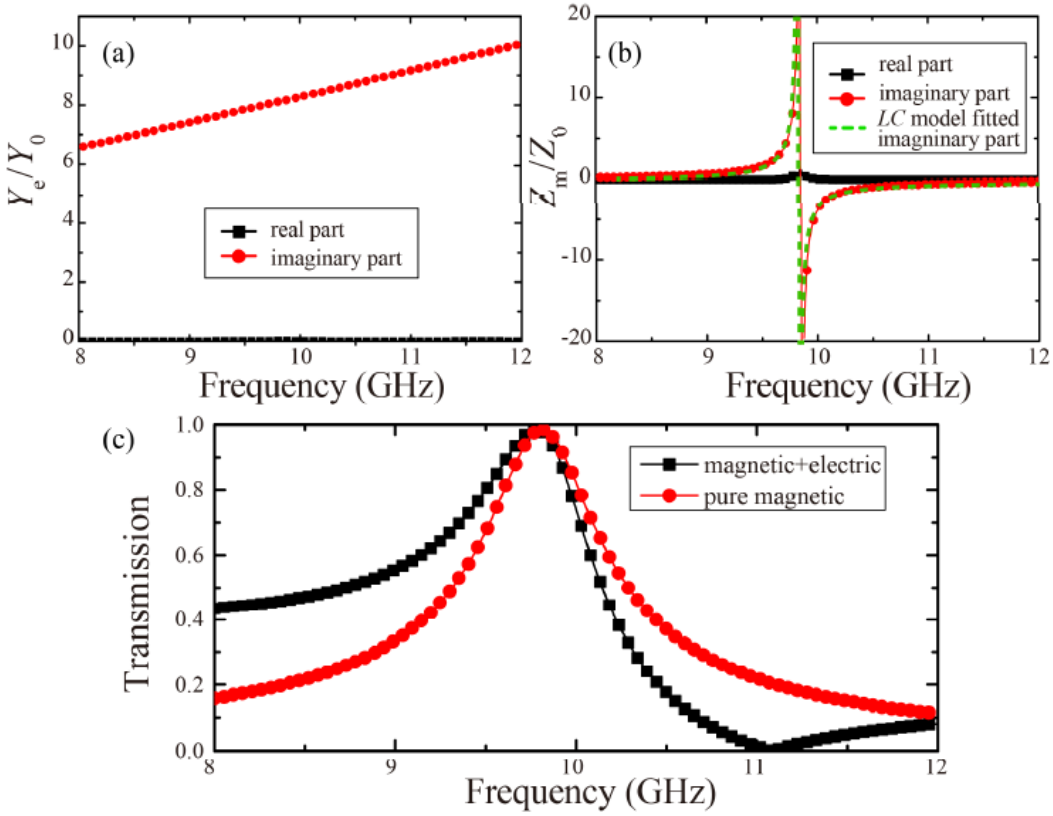

Figure 27: a) Normalized Electric admittance spectrum b) Normalized Magnetic impedance spectrum c) Transmission spectrum when electric admittance and magnetic impedance are included and when just the magnetic impedance is included (Admittance is infinity) *[36]*

Since we can model the transmission coefficient as two parts, each of which is electric admittance and the other is magnetic impedance as depicted in equation (41), the transmission coefficient behaves as a symmetric resonance when there is infinite electric admittance (electric impedance is zero). That means the asymmetric Fano resonance behavior, shown in Figure *27*, is due to the interference between both resonances (electric and magnetic).

$$r = \frac{1}{2}\left(\frac{2Y_0 - Y_e}{2Y_0 + Y_e} + \frac{Z_m - 2Z_0}{Z_m + 2Z_0}\right) \tag{41}$$

$$t = \frac{1}{2}\left(\frac{2Y_0 - Y_e}{2Y_0 + Y_e} - \frac{Z_m - 2Z_0}{Z_m + 2Z_0}\right)$$

For the asymmetric structure, the electric admittance and magnetic impedance, as well as the electric and magnetic sheet currents, are plotted. As the symmetric structure, the electric admittance exhibits a flat frequency response, so it has no resonance. However, the resonance is well-spotted in the magnetic impedance and sheet current, as depicted in Figure *28*. These figures are plotted from the generalized impedance theory.

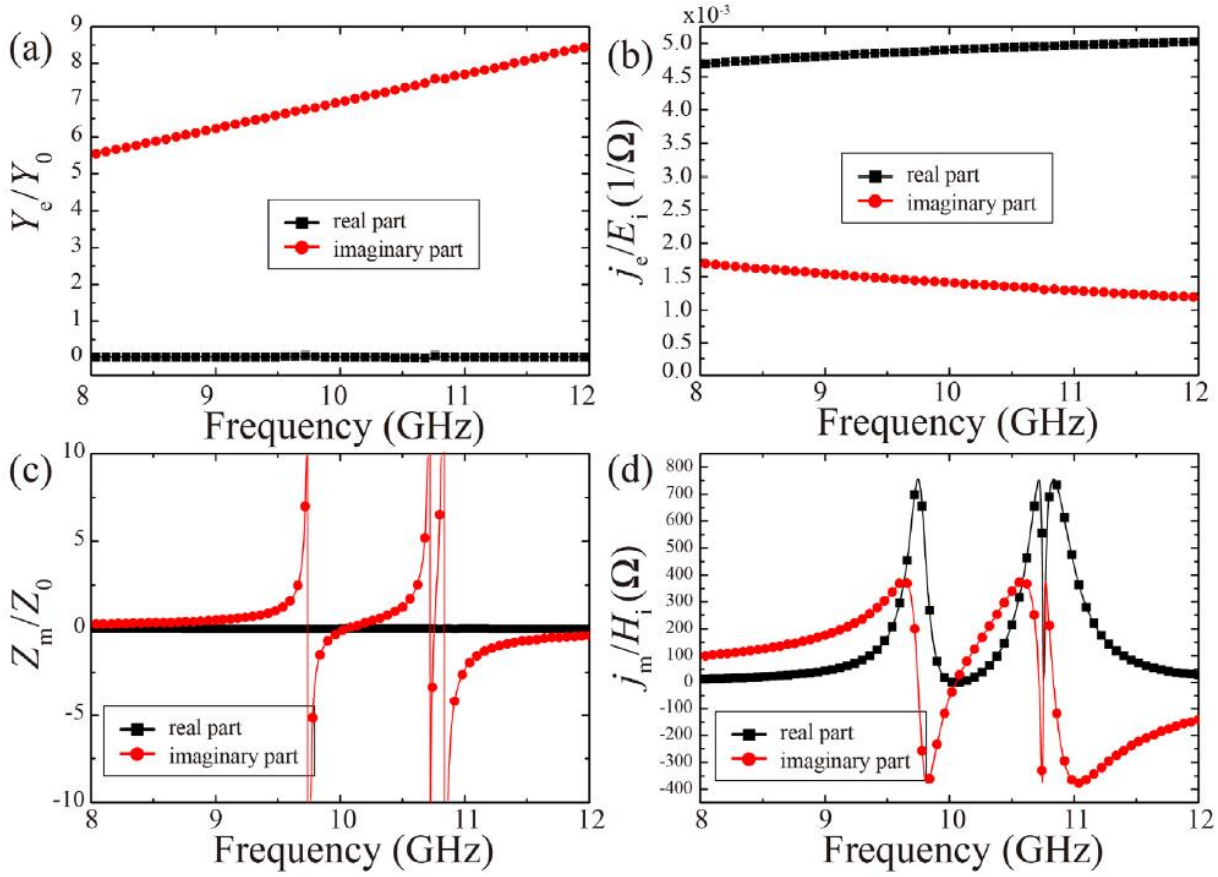

Figure 28: a) Normalized Electric admittance (b) Electric sheet current (c)Normalized Magnetic impedance (d) Magnetic sheet current for asymmetric structure *[36]*.

It is noted that there are three resonant frequencies at $9.79\ GHz, 10.77 GHz\ and\ 10.87 GHz$. The first resonator dominated at the first frequency, while at $10.8 GHz$ the other two resonators dominate. Moreover, between $9.79 GHz < f < 10.77 GHz$ the first resonator's magnetic current is out of phase compared to the other resonators, while between $10.77 GHz < f < 10.87 GHz$, the third resonator is out of phase compared to the other resonators. This result is simulated with

COMSOL Multiphysics and compared with the analytical data. It is found that the simulated results fit entirely with the analytical data as depicted in Figure *29*.

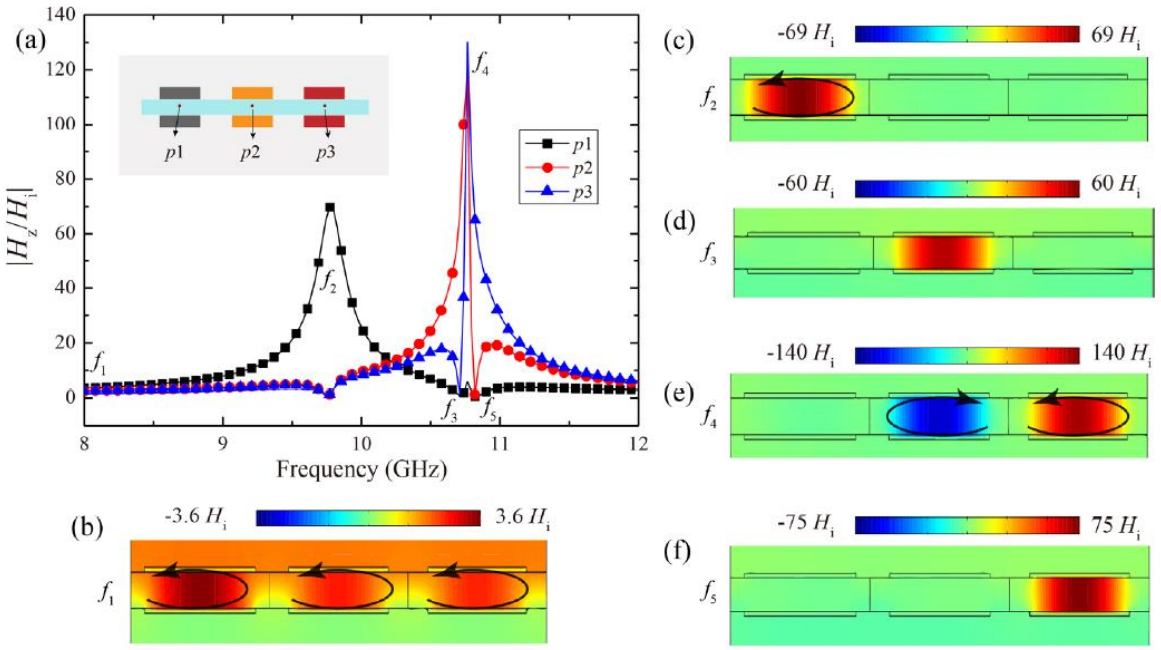

Figure 29: (a) Normalized magnetic fields (Hz) of the three resonators. (b) (c) (d) (e) and (f) show the magnetic field distribution for the three resonators at different frequencies. 8GHz, 9.79GHz, 10.77GHz, 10.82Ghz and 10.87 GHz *[36]*.

In this figure, the magnetic field is obtained for the three resonators at different frequencies. At 8GHz, the three resonators are in phase. However, when the frequency is increased to become 9.79GHz, the first one dominates, as depicted in (c). Moreover, at 10.77GHz, the second resonator dominates, also, between 10.77 GHz and 10.87 GHz, both the second and the third resonator dominate but out of phase. Finally, at 10.87GHz, the third resonator dominates.

All the above analysis was based on neglecting any material loss as the dielectric substrate was lossless, and the wires were PEC. Then, Pu [36] studied the effect of having lossy dielectric substrate and copper with a certain conductivity as a material for the wire structure. As shown in Figure *30*, the transmission and reflection spectrums show evident absorption, which could be used to design wideband absorbers.

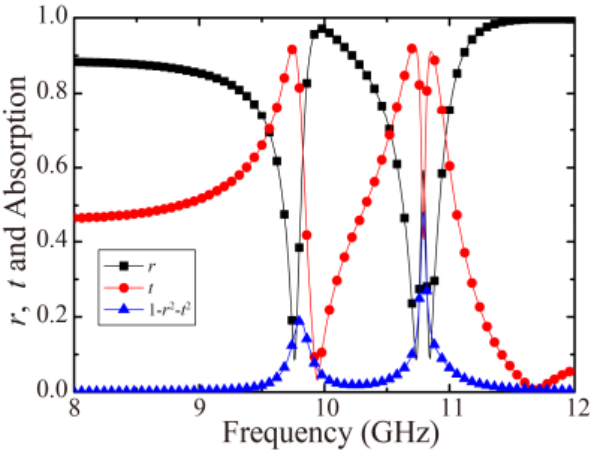

Figure 30: Optical spectrum of the proposed design with lossy materials *[36]*

The general scope of achieving FRs is by breaking the structural symmetry of the unit cell. Worth mentioning here is that Wang et al. [39] were capable of exciting a single FR in a symmetric planar plasmonic structure, as shown in Figure 31 (a), by the coupling between a radiative resonance, represented in the highly-radiative nanorod and known as bright mode and a non-radiative resonance. The incident electromagnetic wave excites the bright mode directly, and the non-radiative dark LC resonance, at which the nanorod represents a central component, is excited by the interaction with the bright resonance in an indirect manner.

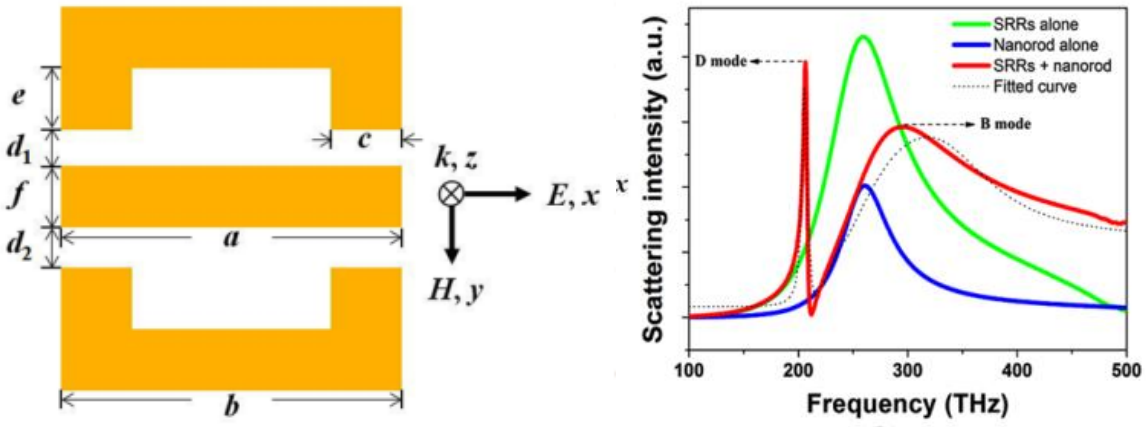

(a) (b)

Figure 31: (a) Schematic of a symmetric two U-shaped SRRs with a nanorod inserted in the middle (b) Spectral scattering response for SRR and nanorod at normal incidence and x-polarized electric field *[39]*. It is important to state that split-ring resonators (SRRs) are essential components of plasmonic metamaterials *[40]*.

Figure *31* (b) illustrates the scattering response of each split ring resonator and the nanorod alone, which exhibits a normal resonant frequency around 260 THz. However, on the introduction of the nanorod between the SRR, a Fano resonance peak and dip appear at 206 THz and 211 THz, respectively, which are known as D mode, in addition to a B mode referring to a normal broad plasmon resonance at 293 THz. Thus, Wang [39] achieved a Fano-resonant-like response in a structure without breaking its symmetry.

Furthermore, Wang [39] studied the tangential current distribution at the normal resonant frequency and the Fano resonance peak frequency, as shown in Figure 32 (a) and (b), respectively. At the normal resonance, the conduction currents in both the nanorod and the SRR are in phase, resembling an electric dipole resonance. However, at the Fano resonance, the currents are parallel but oppositely directed, forming circular currents. That parallel LC resonance, found between the nanorod and each of the SRRs, excites the magnetic dipole resonance. It is essential to mention that two LC resonances are present at the same frequency due to the identical distance between the nanorod and each of the U-shaped split-ring resonators. Thus, the Fano resonance was excited because of the spectral overlap between those electric and magnetic resonances. Both resonances are referred to as bright and dark modes, respectively. Accordingly, it was concluded that the excitation of the Fano-resonance does not merely require breaking the symmetry of a structure. However, it demands coupling between electric and magnetic resonances, which occurs when a common source for both the bright and dark modes exists, which is the nanorod.

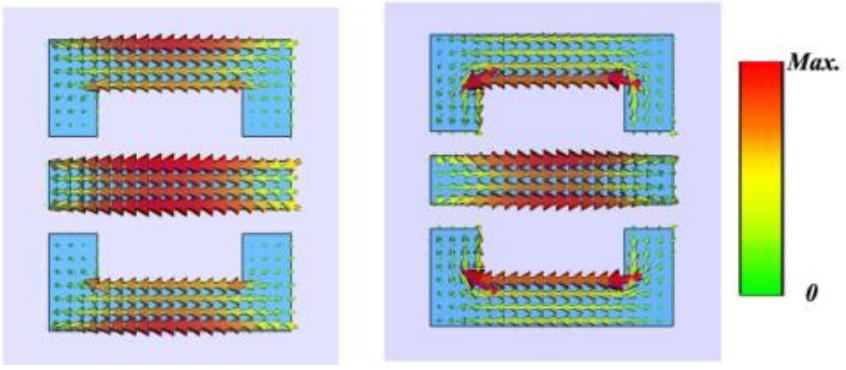

(*a*) (b)

Figure 32: (a) In-phase Tangential Current Distribution at normal resonance (293 THz) (b) Out-of phase Tangential Current Distribution at Fano-resonant frequency (206 THz) *[39]*

When Wang [39] broke this symmetry by changing the coupling length between the nanorod and the two SRRs, two Fano resonances were achieved, as shown in Figure *33*, as the magnetic dipole resonance takes place at different frequencies. The first Fano resonance denoted as D_1 mode occurs at $206\ THz$ and the second one, denoted as D_2 mode, arises at $218\ THz$.

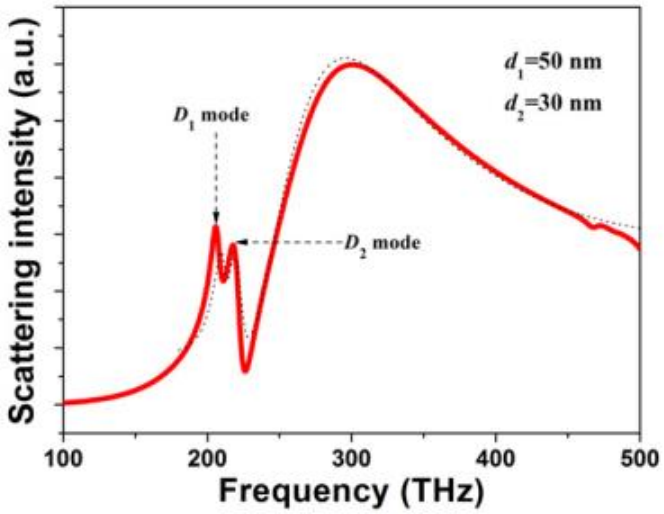

Figure 33: Spectral scattering response for asymmetric SRRs and nanorod at normal incidence and x-polarized electric field *[39]*

In 2020, Long et al. [41] utilized a similar concept to achieve a sharp FR response in an all-dielectric metasurface composed of non-symmetric double silicon nanorods, as shown in Figure *34*. Such design was able to achieve high-quality factor by omitting the radiative losses usually associated with metals in different frequency regimes.

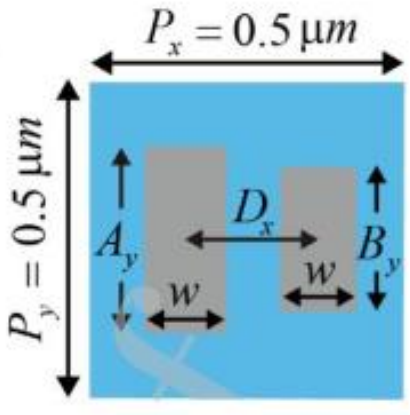

Figure 34: Schematic of Asymmetric double nanorods unit cell *[41]*

As demonstrated in Figure 35, a Fano resonance can be observed at the quadrupole at both TE and TM modes at 916 nm and 1029 nm respectively with approximately 100% reflection and transmission and exceptionally high Q-factor.

Like the analysis mentioned in previous work, the normal resonance, which is termed "dipole" in this paper, is excited on the direct interaction of the asymmetric structure with the incident wave. At the same time, this incident EM wave excites indirectly the dark mode resonance, which is known in this paper as quadrupole mode, by coupling with the bright mode. These two modes couple with each other destructively and results in the excitation of the Fano resonance. Moreover, the field distribution of E_z at the dipole mode shows in phase induced currents; however, at quadrupole, the induced currents are out of phase. Accordingly, the coupling between both modes gives rise to the Fano resonance. Thus, the dipole and quadrupole can be referred to as bright and dark modes, respectively.

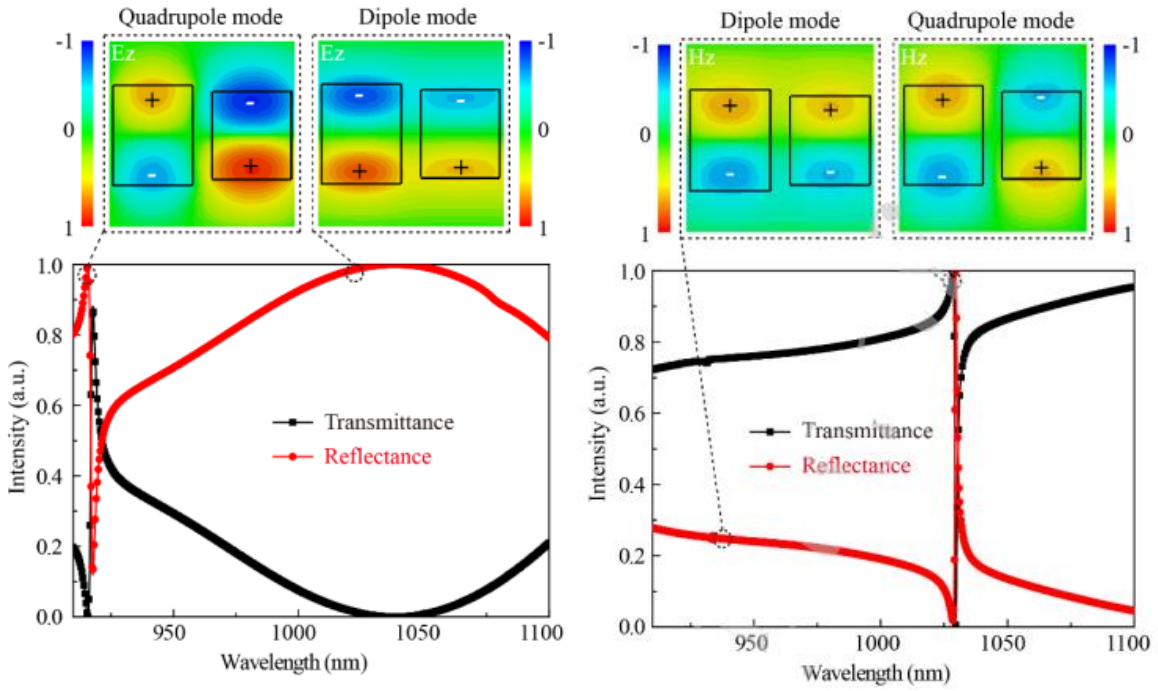

Figure 35: (a) Spectral TE mode response and real E_z field component at quadrupole ($\lambda = 916\ nm$) and dipole resonances ($\lambda = 1029\ nm$) (b) Spectral TM mode response and real H_z field component at quadrupole ($\lambda = 1029\ nm$)and dipole resonances ($\lambda = 936\ nm$) *[41]*

Figure *36* shows a parametric sweep, studying the effect of the degree of symmetry on the spectral response, where the length of one of the nanorods was changed while keeping the other fixed at $0.25\,\mu m$. The absence of the Fano resonance was observed on having a symmetric structure. As the length of the nanorod increases, the resonant wavelength was red-shifted with a broad spectrum. Furthermore, while studying the effect of implementing lossy materials, Long [41] proved that it only affects the reflection and transmission spectrum intensity.

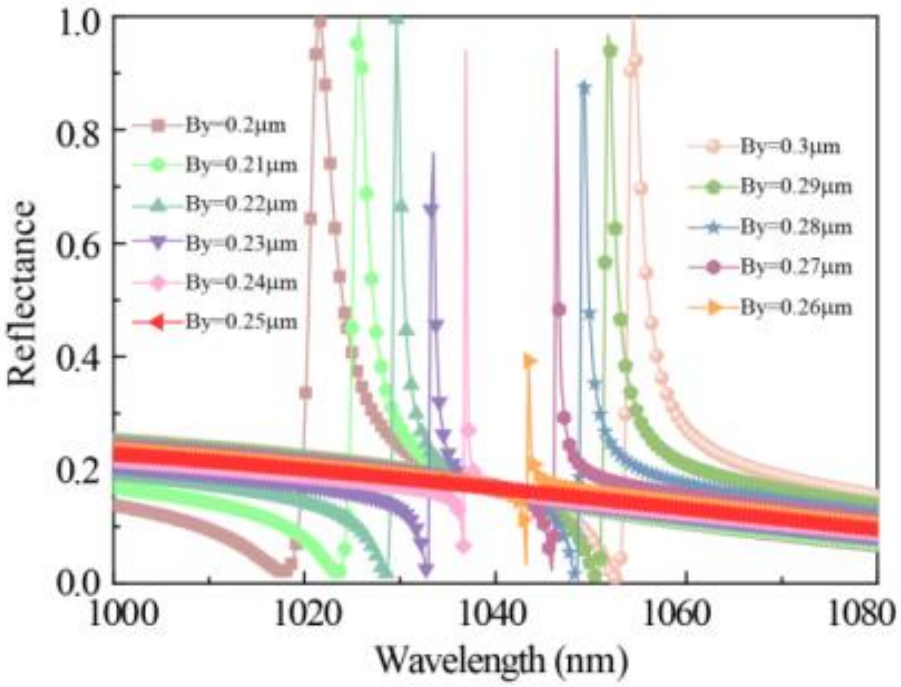

Figure 36: Parametric Sweep of different lengths of one of the nanorods, while the length of the other rod is fixed at $0.25\,\mu m$ *[41]*

Chapter 4

4. Cross-junction based metasurface

This chapter presents the research work that has been done, in which a design for an electromagnetic metasurface in the microwave regime has been proposed. The purpose of this work is to observe and investigate the presence of Fano resonance in the microwave regime. In addition to a parametric sweep over the degree of the asymmetry, the simulated structure performance has been studied using both CST Studio Suite® and Ansys HFSS. Then, the theory and physical concept behind such performance have been analyzed. The design has been fabricated and characterized inside an anechoic chamber. Both numerical and measured data show to be in perfect agreement.

4.1 Proposed Design

In this work, we present a unit cell consisting of an asymmetric metallic cross-junction surrounded by four square patches over a thin subwavelength substrate. The unit cell is chosen to have a square footprint with a pitch of $22.86\,mm$ throughout the work. A schematic of the proposed unit cell is shown in Figure *37*(a), which shows the proposed unit cell with all the relevant dimensions used in our work to manipulate the electromagnetic response of the metasurface. Figure *37* (a) and (b) show alternative perspectives for the unit cell that are useful in visualizing and interpreting the unit cell behavior, as shown in the following sections. In the simulations, the metal is assumed to be a perfect electric conductor (PEC), and the substrate is chosen to be a dielectric of permittivity 4.4. The thickness of the substrate is $1.57\,mm$, and the side length of the square patches (W) is $5.5\,mm$. Figure 38 shows several screenshots of the simulated unit cell on CST with two different perspective views.

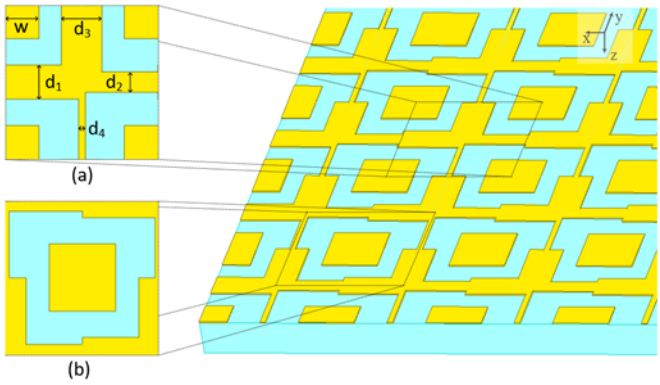

Figure 37: Schematic of the proposed periodic structure, where (a) is the unit cell in cross junction perspective and (b) is the unit cell in the asymmetric ring and patch perspective.

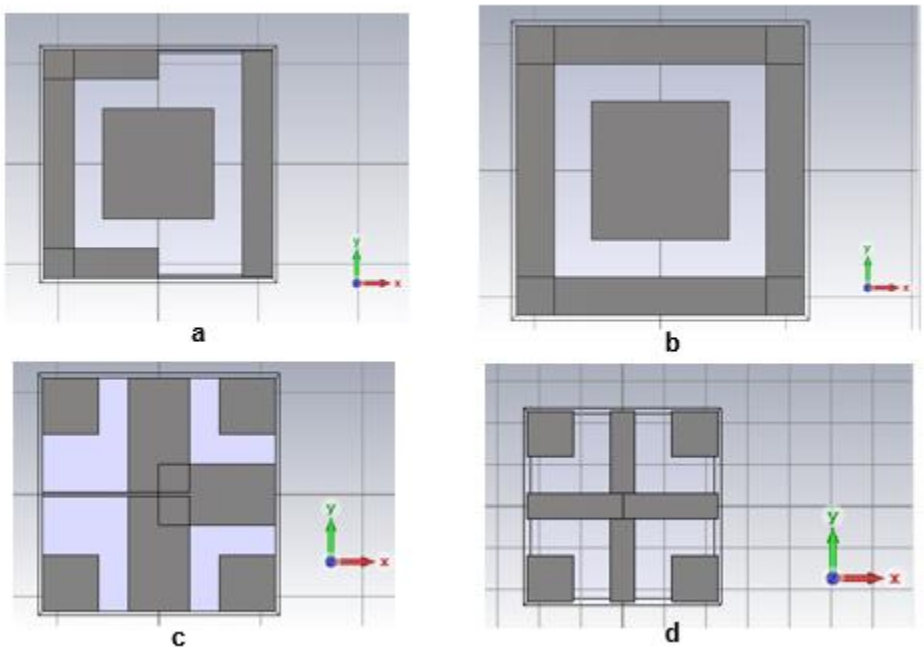

Figure 38: CST screenshots for the schematic of the unit cell (a) asymmetric structure in the ring and patch perspective (b) symmetric structure in the ring and patch perspective (c) asymmetric structure in the cross junction perspective (d) *) symmetric structure in the* cross junction perspective

4.2 Theory and Analysis

Firstly, we study the behavior of the symmetric unit cell, in which all stubs' thicknesses (d_1, d_2, d_3, d_4) are of the same width that is set to 6 mm. The unit cell is surrounded by periodic boundary conditions in all the simulations and is excited by a normally incident plane wave, as shown in Figure 39 and Figure 40, respectively.

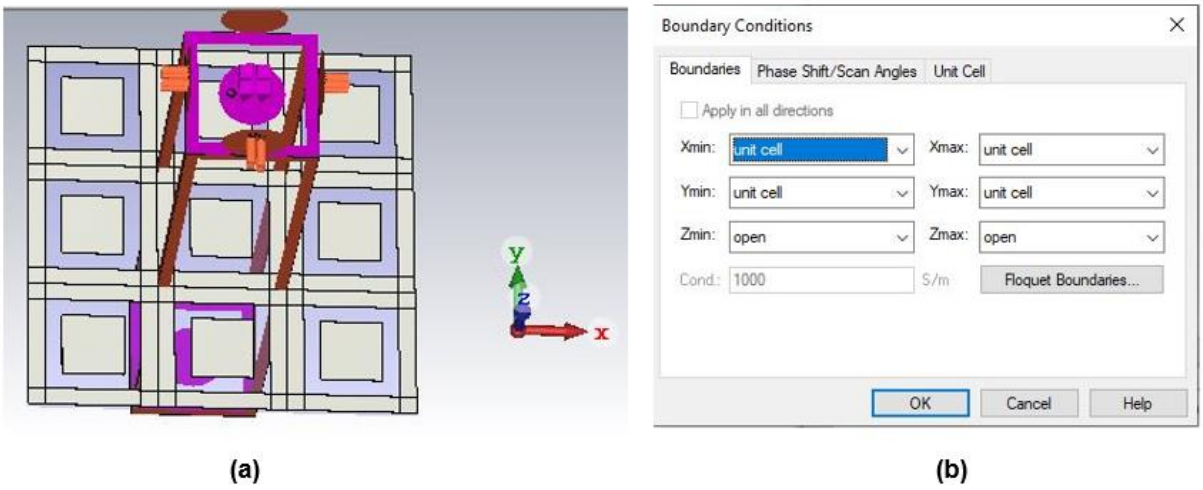

Figure 39: (a) Periodic array of the simulated unit cells. (b) Periodic Boundary conditions

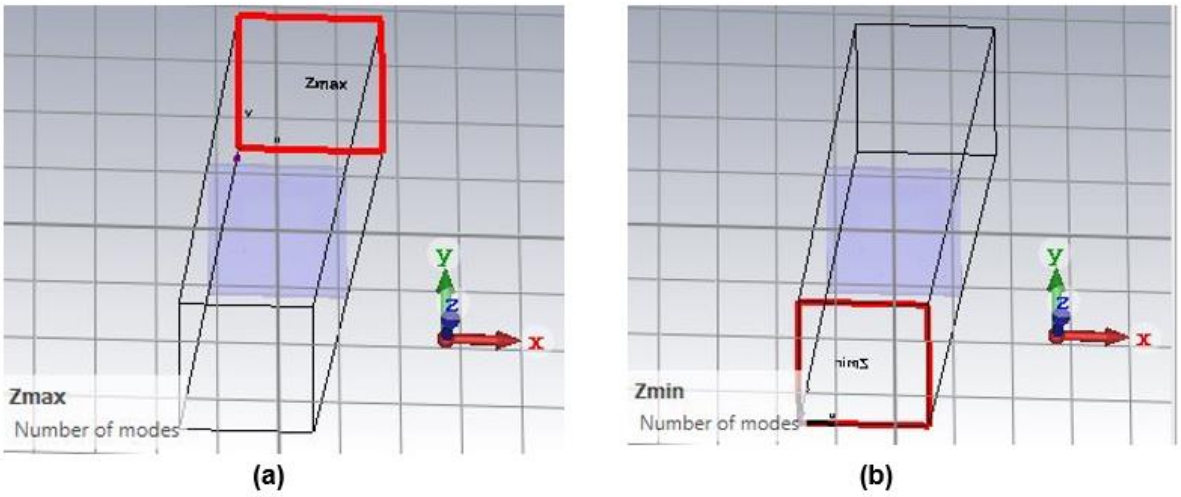

Figure 40: (a) Port (1) and (b) Port (2) in CST

As shown in Figure *41*, the magnitude of the reflection coefficient |R| shows two distinct resonances at 5 GHz and 11.4 GHz. This spectral profile is shown for an incident wave whose electric field is polarized along the x-direction. Obviously, in this configuration, the polarization of the incident electric field does not affect the response of the metasurface due to the structural symmetry of the unit cell. Next, we introduced structural asymmetry to the unit cell and investigated the effect of such asymmetry on the spectral behavior of the metasurface. In this case, we fixed d_2, d_3 and d_4 to be 6 mm and changed d_1 to be 0.4 mm. As shown in Figure *41*, the asymmetric cross-junction retains the two resonances previously exhibited by the symmetric

unit cell at 3.8 GHz and 11.6 GHz. This slight shift to a lower frequency is because the electrical path increased. Interestingly, when the polarization of the electric field of the incident wave was set to be along the direction of the variation of arms' widths (x-direction), a distinct FR reveals itself at around 6.7 GHz, achieving a quality factor of 122.24.

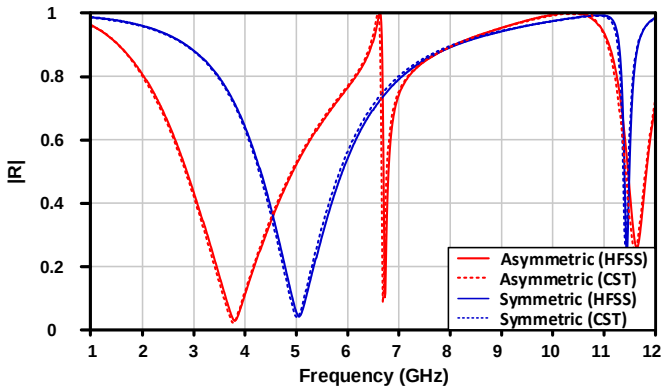

Figure 41: Simulated |R| for the symmetric and asymmetric unit cell.

Figure 42 (a) and (b) show the y and x polarized electric fields, respectively. It is worth mentioning that the different field orientations will react similarly in the symmetric structure. In Figure 43(a), both the y and x oriented fields have the same profile since the structure is symmetric. However, on having a structure asymmetry, the FR only appeared in the X-oriented since breaking the symmetry was along the x-axis and it did not appear in the y-orientation as shown in Figure 43(b). So, breaking the symmetry allowed only a certain mode in a certain orientation to couple with the bright mode and generated the FR.

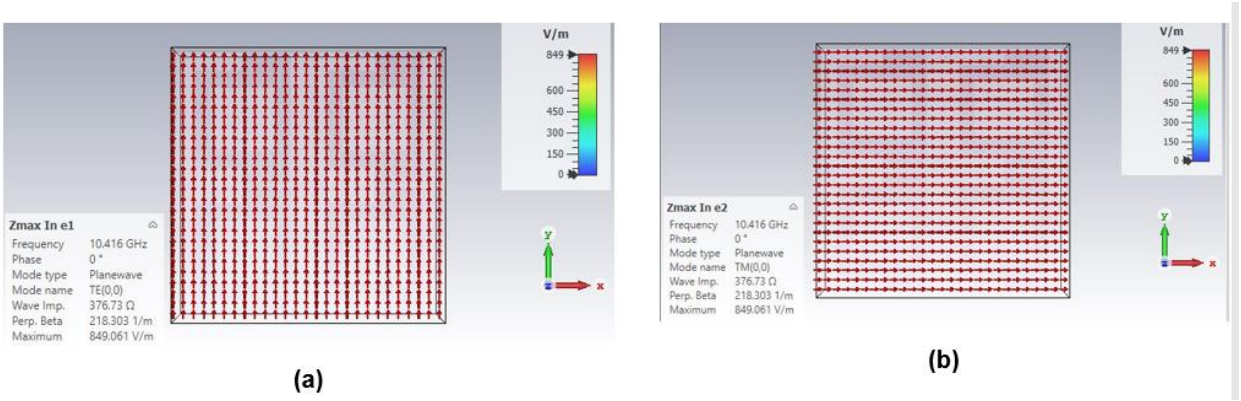

Figure 42: (a) Y-polarized Electric Field (b) X-polarized Electric Field

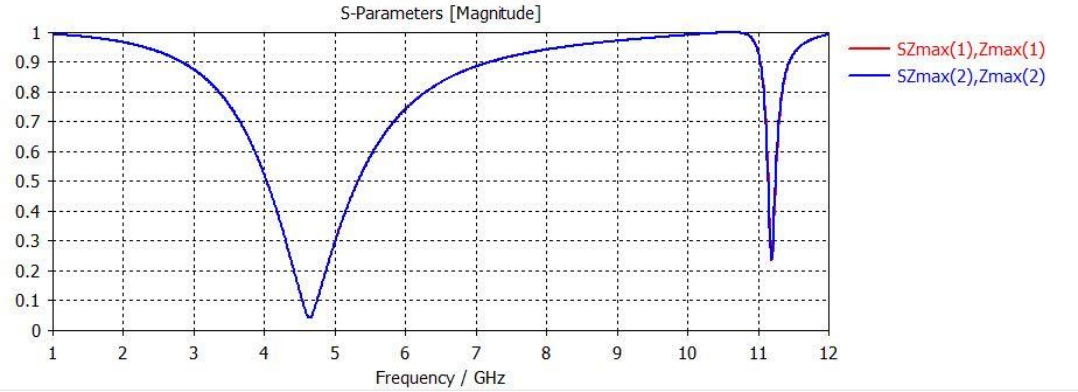

(a)

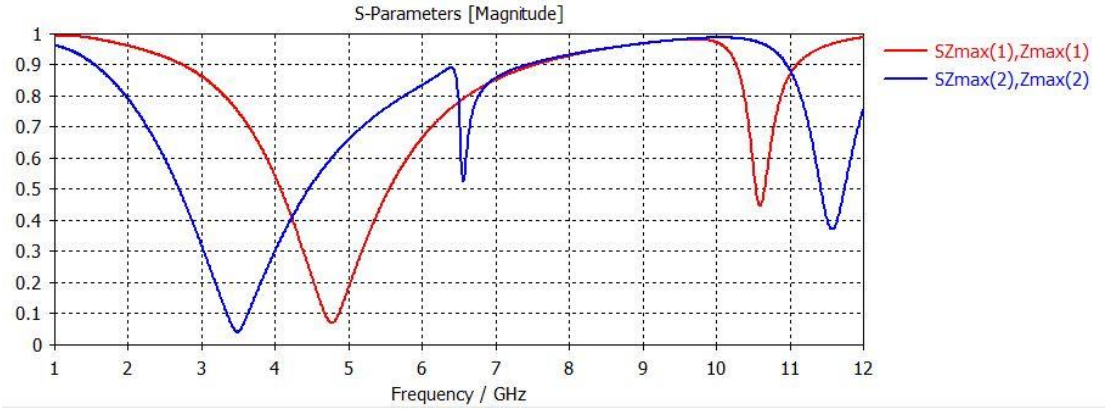

(b)

Figure 43: (a) S_{11} parameter for both the x and y oriented field in symmetric structure (b) S_{11} parameter for the x and y oriented field in an asymmetric structure

In order to better understand the physical origin of this sharp FR, we investigate the field distribution on the structure in the x-y plane. The bright modes corresponding to the electric dipoles show up as transmission peaks both in the symmetric and asymmetric designs, as shown in Figure *41*. Furthermore, the dark mode corresponding to the quadrupole mode appears as a transmission peak in the asymmetric structure. Figure *44* (a) and (b) show the z component of the magnetic field distribution in the x-y plane for the first bright mode in the symmetric and asymmetric structures at $5\ GHz$ and $3.8\ GHz$, respectively. Obviously, both the symmetric and asymmetric structures support in-phase conduction currents at those frequencies. Like an electric dipole oscillation, those correspond to a broad bright mode due to the radiative damping.

For the FR at $6.7\ GHz$ (Dark mode), anti-parallel oscillation currents are observed. Corresponding magnetic field component H_z in the x-y plane is presented in Figure *44* (c). At

this resonance, the structure is weakly coupled to the free space. If we imagined this eigenmode in a symmetric structure, it would exhibit the same profile but with equal amplitude. So, applying the right-hand rule would generate currents equal in magnitude and opposite in direction, thus canceling each other, which describes the disappearance of this mode in the symmetric structure. Once we broke the symmetry, these magnitudes differed, and the FR evolved from the interaction and coupling between the bright and dark modes in the structure at 6.7 GHz.

In the present metasurface, the dipolar resonance of the unit cell represents the bright mode, and the symmetry breaking leads to the excitation of the dark subradiant mode. The coupling between these two modes leads to the FR in the transmission spectra of the metasurface. The same approach mentioned for the first bright mode is applicable for the second bright modes in the symmetric and asymmetric structures at 11.4 GHz and 11.6 GHz, respectively, which are regarded as higher-order modes of the first bright modes as shown in Figure *44* (d) and (e).

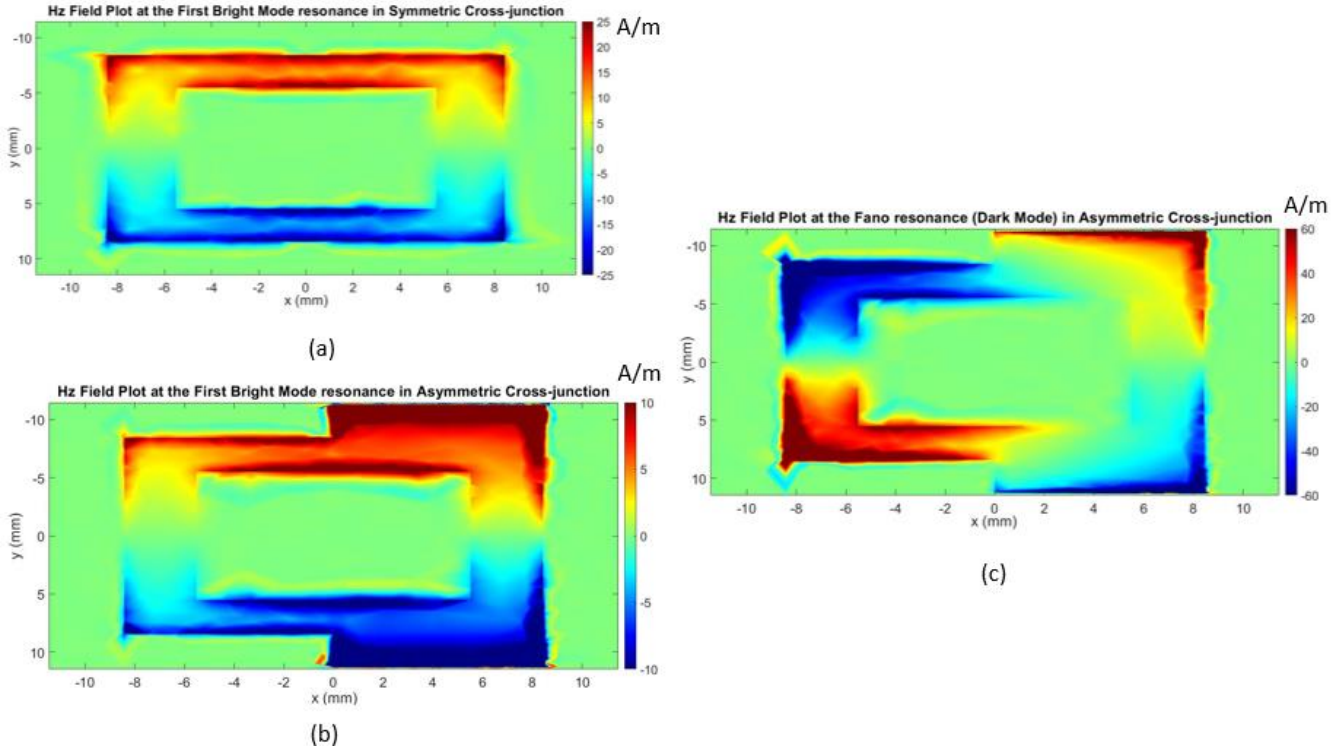

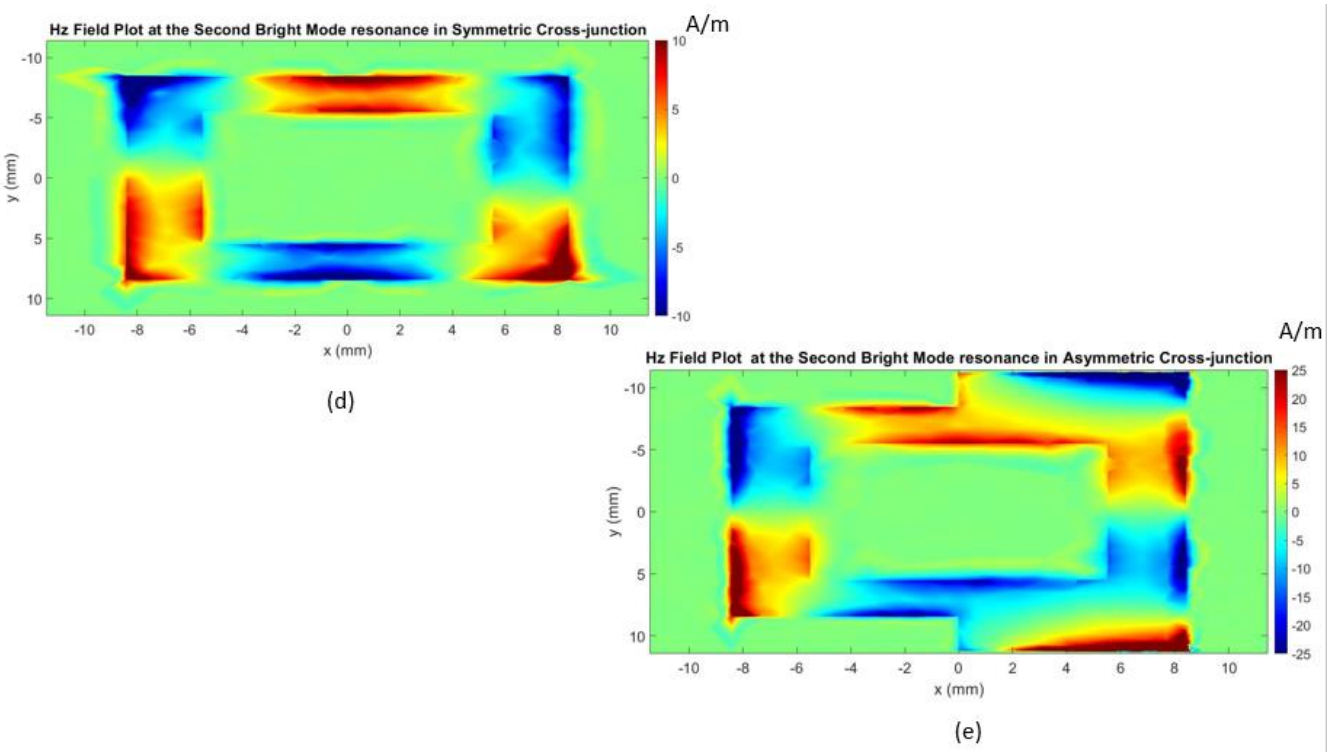

Figure 44: Magnetic field distribution (H_z) for the first bright mode in (a) symmetric and (b) asymmetric ring-patch. (c) Magnetic field distribution (H_z) at FR asymmetric ring-patch Magnetic field distribution (H_z) for the second bright mode in (d) symmetric and (e) asymmetric ring-patch.

4.3 Simulation Results

Next, we perform a parametric study to inspect the effect of the degree of asymmetry through changing d_1 on the spectral response of the metasurface. As can be seen in Figure *45*, three arms of the cross were set to $6\,mm$ width, and d_1 is initially set to be $0.4\,mm$, and its value is incremented in linear steps. This study aims to observe and investigate the evolution of the FR as the structural asymmetry is reduced until the unit cell becomes symmetric. As depicted in Figure *45*(a), as the structural asymmetry is decreased, the FR shifts to a higher frequency as the electrical size of the unit cell decreases. Also, as the structural asymmetry is reduced, the resonance becomes of higher Q. As shown in Figure *45*(b), the bandwidth of the FR becomes so small as the degree of asymmetry decreases, it becomes approximately zero, thus giving a very high Q. Accordingly, this means that the range of frequencies at which the bright and dark modes couple with each other becomes very narrow until it reaches zero. And the frequency does not increase with the same ratio. So, if we calculated the quality factors, it will become of high value. Furthermore, as the structure becomes symmetric (d_1=6 mm), the FR disappears.

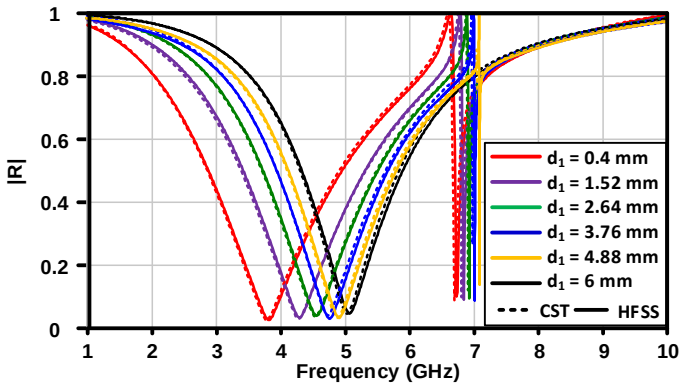

(a)

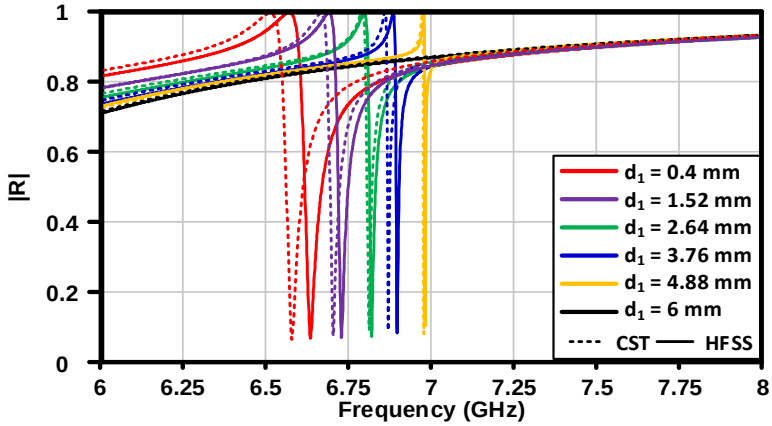

(b)

Figure 45: (a) |R| of the asymmetric unit cell at different arm widths over a wide bandwidth, (b) and over narrow bandwidth around the Fano resonance

4.4 Fabricated Results and Measurements

This section shed some light on the experimental setup we utilized to characterize our proposed structure. We fabricated the metasurface whose constituent unit cell having $d_2 = d_3 = d_4 = 6\,mm$. d_1 was set to be 0.4 mm, as shown in Figure *46*. As shown in Figure *46*(a), the fabricated sample contains 10×13 unit cells, with a total size of about $6237\ (210\ x\ 297)\ mm^2$. The patches and the stubs are made of copper etched on top of FR4 dielectric substrate of thickness 1.57 mm and dielectric permittivity of 4.4 and loss tangent of 0.02.

The measurement was carried out at an anechoic chamber (see Figure *46*(a)). As a far-field characterization process, we shine the metasurface by a plane wave emitted from a linear-polarization horn antenna. At the other side of the metasurface, we placed another identical horn antenna. The transmitting and receiving antennas were perfectly aligned. The scattering matrix of the structure was characterized using a network analyzer.

Figure *46*(b) shows the measured response of the metasurface in comparison with the simulated response in CST Studio Suite® and Ansys HFSS. The measured results show excellent agreement with the numerical simulations. These losses and low-quality factor are due to the use of a lossy substrate. FR4 is the cheapest substrate, and at the same time, we wanted to have a large size of the structure to resemble the periodic boundary condition. So, to compromise between the cost and the size, we chose FR4. Although there were other substrates with better performance, they were expensive. We were only trying to prove the concept with the least price.

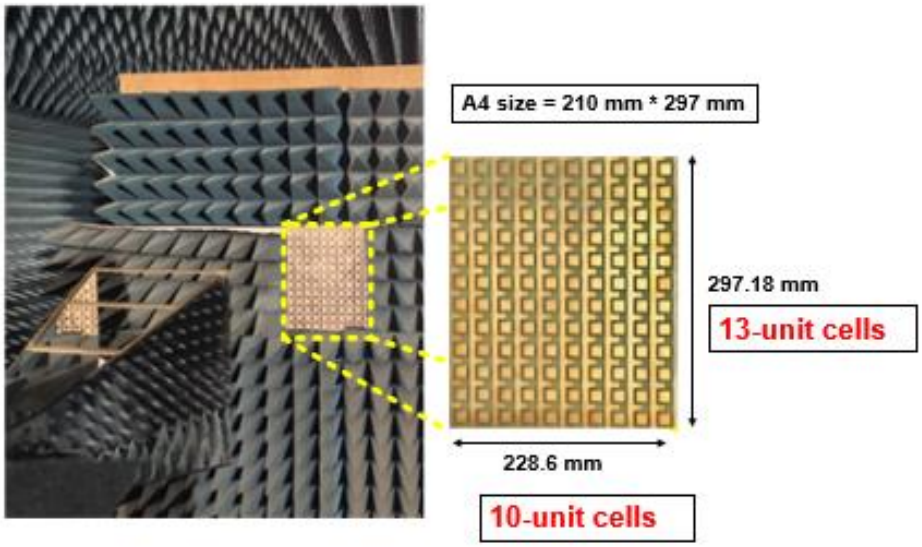

(a)

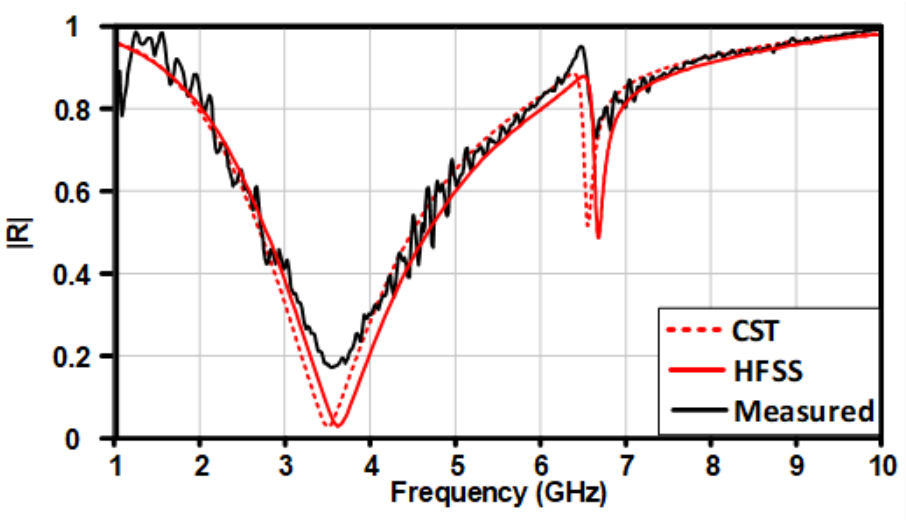

(b)

Figure 46:(a) Measurement setup and the fabricated metasurface, (b) Simulated and experimentally measured magnitude of the reflection coefficient |R|.

Chapter 5

5. Conclusion and Future Work

This chapter recaps all the information that was mentioned in the previous chapters. In addition, future work is also presented.

5.1 Conclusion

In chapter (1), a summary of the conventional materials that existed before metamaterials and their limitations that gave rise to the development of metamaterials and their salient role has been introduced. Then, an introduction of metamaterials and the evolution of these 3D structures to 2D, known as metasurfaces, have been presented. Furthermore, a glance at Fano resonance has been discussed.

Chapter (2) demonstrates the physical fundamentals guiding the metamaterials and metasurfaces' performance, including the generalized laws of reflection and refraction. In addition, a comparison between metamaterials and photonic/electronic bandgap materials, in addition to a comparison between metasurfaces and frequency-selective surfaces, has been shown.

Chapter (3) is a literature review for previous work on the application of metasurfaces in different fields and the progress of Fano resonance in numerous applications.

In Chapter (4), my research work is presented, in which a unit cell has been proposed, resulting in the excitation of a single sharp FR by breaking the structural symmetry in a single layer cross-junction based metasurface structure owing to the interaction between the bright and dark modes. The spectral response of the proposed design has been studied. Furthermore, the system was fabricated and characterized. The simulated and measured results prove to be in good agreement with each other.

5.2 Future Work

It is intended to apply the proposed design in real-time applications and study its performance. These applications could include refractive-index sensing applications, which will be mainly concerned with bio-sensing to check its efficiency and sensitivity. Another application is polarization rotation and chirality, at which the polarization of the incident wave could be changed.

Moreover, an RLC circuit model will be designed to represent the source of resonance in the structure and represent it theoretically. The temporal coupled-mode theory is an abstract model. It would be beneficial to reach a relation joining between the coupling and the structure geometry. For instance, if we want to increase the coupling between the bright and dark modes, we will change the stub width or the patch size. We aim to reach a closed-form equation describing the structure geometry before simulating with CST or HFSS.

Furthermore, on inserting two-unit cells inside a rectangular waveguide while studying the behavior of the proposed design, a unique behavior was observed. Although it is known that no wave can propagate before the cut-off frequency of the waveguide, a sharp resonance was noticed. Such peculiar behavior needs further investigation and analysis.

References

[1] N. Engheta and R. W. Ziolkowski, “Physics and Engineering Explorations,” p. 438.

[2] C. Caloz and T. Itoh, *Electromagnetic Metamaterials: Transmission Line Theory and Microwave Applications: The Engineering Approach*. Hoboken, NJ, USA: John Wiley & Sons, Inc., 2005. doi: 10.1002/0471754323.

[3] S. Zouhdi, A. Sihvola, and M. Arsalane, Eds., *Advances in Electromagnetics of Complex Media and Metamaterials*. Dordrecht: Springer Netherlands, 2002. doi: 10.1007/978-94-007-1067-2.

[4] I. V. Lindell, A. H. Sihvola, and J. Kurkijarvi, “Karl F. Lindman: the last Hertzian, and a harbinger of electromagnetic chirality,” *IEEE Antennas Propag. Mag.*, vol. 34, no. 3, pp. 24–30, Jun. 1992, doi: 10.1109/74.153530.

[5] N. Engheta, “An idea for thin subwavelength cavity resonators using metamaterials with negative permittivity and permeability,” *Antennas Wirel. Propag. Lett.*, vol. 1, pp. 10–13, 2002, doi: 10.1109/LAWP.2002.802576.

[6] H. Lamb, “On Group - Velocity,” *Proceedings of the London Mathematical Society*, vol. s2-1, no. 1, pp. 473–479, 1904, doi: 10.1112/plms/s2-1.1.473.

[7] C. L. Holloway, E. F. Kuester, J. A. Gordon, J. O’Hara, J. Booth, and D. R. Smith, “An Overview of the Theory and Applications of Metasurfaces: The Two-Dimensional Equivalents of Metamaterials,” *IEEE Antennas Propag. Mag.*, vol. 54, no. 2, pp. 10–35, Apr. 2012, doi: 10.1109/MAP.2012.6230714.

[8] B. B. Tierney, N. I. Limberopoulos, R. L. Ewing, and A. Grbic, “A Planar, Broadband, Metamaterial-Based, Transmission-Line Beamformer,” *IEEE Trans. Antennas Propagat.*, vol. 66, no. 9, pp. 4844–4853, Sep. 2018, doi: 10.1109/TAP.2018.2845444.

[9] N. I. Landy, S. Sajuyigbe, J. J. Mock, D. R. Smith, and W. J. Padilla, “Perfect Metamaterial Absorber,” *Phys. Rev. Lett.*, vol. 100, no. 20, p. 207402, May 2008, doi: 10.1103/PhysRevLett.100.207402.

[10] O. Quevedo-Teruel *et al.*, “Roadmap on metasurfaces,” *J. Opt.*, vol. 21, no. 7, p. 073002, Jul. 2019, doi: 10.1088/2040-8986/ab161d.

[11] A. Li, S. Singh, and D. Sievenpiper, “Metasurfaces and their applications,” p. 23.

[12] N. Yu *et al.*, “Light Propagation with Phase Discontinuities: Generalized Laws of Reflection and Refraction,” *Science*, vol. 334, no. 6054, pp. 333–337, Oct. 2011, doi: 10.1126/science.1210713.

[13] D. F. Sievenpiper, J. H. Schaffner, H. J. Song, R. Y. Loo, and G. Tangonan, “Two-dimensional beam steering using an electrically tunable impedance surface,” *IEEE Trans.*

Antennas Propagat., vol. 51, no. 10, pp. 2713–2722, Oct. 2003, doi: 10.1109/TAP.2003.817558.

[14] J. Lin, P. Genevet, M. A. Kats, N. Antoniou, and F. Capasso, "Nanostructured Holograms for Broadband Manipulation of Vector Beams," *Nano Lett.*, vol. 13, no. 9, pp. 4269–4274, Sep. 2013, doi: 10.1021/nl402039y.

[15] Caiazzo, Maci, and Engheta, "A metamaterial surface for compact cavity resonators," *Antennas Wirel. Propag. Lett.*, vol. 3, pp. 261–264, 2004, doi: 10.1109/LAWP.2004.836576.

[16] N. Yu, Q. Wang, and F. Capasso, "Beam engineering of quantum cascade lasers," *Laser & Photon. Rev.*, vol. 6, no. 1, pp. 24–46, Jan. 2012, doi: 10.1002/lpor.201100019.

[17] D. Schurig *et al.*, "Metamaterial Electromagnetic Cloak at Microwave Frequencies," *Science*, vol. 314, no. 5801, pp. 977–980, Nov. 2006, doi: 10.1126/science.1133628.

[18] R. Singh *et al.*, "Observing metamaterial induced transparency in individual Fano resonators with broken symmetry," *Appl. Phys. Lett.*, vol. 99, no. 20, p. 201107, Nov. 2011, doi: 10.1063/1.3659494.

[19] W. Cao, R. Singh, C. Zhang, J. Han, M. Tonouchi, and W. Zhang, "Plasmon-induced transparency in metamaterials: Active near field coupling between bright superconducting and dark metallic mode resonators," *Appl. Phys. Lett.*, vol. 103, no. 10, p. 101106, Sep. 2013, doi: 10.1063/1.4819389.

[20] Y. Yao *et al.*, "Electrically Tunable Metasurface Perfect Absorbers for Ultrathin Mid-Infrared Optical Modulators," *Nano Lett.*, vol. 14, no. 11, pp. 6526–6532, Nov. 2014, doi: 10.1021/nl503104n.

[21] U. Fano, "Effects of Configuration Interaction on Intensities and Phase Shifts," *Phys. Rev.*, vol. 124, no. 6, pp. 1866–1878, Dec. 1961, doi: 10.1103/PhysRev.124.1866.

[22] H.-T. Chen, A. J. Taylor, and N. Yu, "A review of metasurfaces: physics and applications," *Rep. Prog. Phys.*, vol. 79, no. 7, p. 076401, Jul. 2016, doi: 10.1088/0034-4885/79/7/076401.

[23] N. Yu and F. Capasso, "Flat optics with designer metasurfaces," *Nature Mater*, vol. 13, no. 2, pp. 139–150, Feb. 2014, doi: 10.1038/nmat3839.

[24] M. Abdelsalam, A. M. Mahmoud, and M. A. Swillam, "Polarization independent dielectric metasurface for infrared beam steering applications," *Sci Rep*, vol. 9, no. 1, p. 10824, Dec. 2019, doi: 10.1038/s41598-019-47097-5.

[25] Z. Wang, Y. Sun, L. Han, and D. Liu, "General laws of reflection and refraction for subwavelength phase grating," p. 12.

[26] K. Sarabandi and N. Behdad, “A Frequency Selective Surface With Miniaturized Elements,” *IEEE Trans. Antennas Propagat.*, vol. 55, no. 5, pp. 1239–1245, May 2007, doi: 10.1109/TAP.2007.895567.

[27] S. S. Bukhari, J. Vardaxoglou, and W. Whittow, “A Metasurfaces Review: Definitions and Applications,” *Applied Sciences*, vol. 9, no. 13, p. 2727, Jul. 2019, doi: 10.3390/app9132727.

[28] H. A. Haus, *Waves and Fields in Optoelectronics*. Prentice Hall, 1984.

[29] A. Khanikaev, C. Wu, and G. Shvets, “Fano-resonant metamaterials and their applications,” *Nanophotonics*, vol. 2, pp. 247–264, 2013.

[30] F. Monticone, N. M. Estakhri, and A. Alù, “Full Control of Nanoscale Optical Transmission with a Composite Metascreen,” *Phys. Rev. Lett.*, vol. 110, no. 20, p. 203903, May 2013, doi: 10.1103/PhysRevLett.110.203903.

[31] C. Pfeiffer and A. Grbic, “Metamaterial Huygens’ Surfaces: Tailoring Wave Fronts with Reflectionless Sheets,” *Phys. Rev. Lett.*, vol. 110, no. 19, p. 197401, May 2013, doi: 10.1103/PhysRevLett.110.197401.

[32] C. Pfeiffer, N. K. Emani, A. M. Shaltout, A. Boltasseva, V. M. Shalaev, and A. Grbic, “Efficient Light Bending with Isotropic Metamaterial Huygens’ Surfaces,” *Nano Lett.*, vol. 14, no. 5, pp. 2491–2497, May 2014, doi: 10.1021/nl5001746.

[33] V. A. Fedotov, M. Rose, S. L. Prosvirnin, N. Papasimakis, and N. I. Zheludev, “Sharp Trapped-Mode Resonances in Planar Metamaterials with a Broken Structural Symmetry,” *Phys. Rev. Lett.*, vol. 99, no. 14, p. 147401, Oct. 2007, doi: 10.1103/PhysRevLett.99.147401.

[34] F. Hao, Y. Sonnefraud, P. V. Dorpe, S. A. Maier, N. J. Halas, and P. Nordlander, “Symmetry Breaking in Plasmonic Nanocavities: Subradiant LSPR Sensing and a Tunable Fano Resonance,” *Nano Lett.*, vol. 8, no. 11, pp. 3983–3988, Nov. 2008, doi: 10.1021/nl802509r.

[35] A. Christ, O. J. F. Martin, Y. Ekinci, N. A. Gippius, and S. G. Tikhodeev, “Symmetry Breaking in a Plasmonic Metamaterial at Optical Wavelength,” *Nano Lett.*, vol. 8, no. 8, pp. 2171–2175, Aug. 2008, doi: 10.1021/nl0805559.

[36] M. Pu *et al.*, “Investigation of Fano resonance in planar metamaterial with perturbed periodicity,” *Opt. Express*, vol. 21, no. 1, p. 992, Jan. 2013, doi: 10.1364/OE.21.000992.

[37] Y. Joe, A. Satanin, and C. Kim, “Classical analogy of Fano resonances,” *Physica Scripta*, vol. 74, no. 2, pp. 259–266, 2006.

[38] B. Gallinet and O. Martin, “Ab initiotheory of Fano resonances in plasmonic nanostructures and metamaterials,” *Physical Review B*, vol. 83, no. 23, 2011.

[39] J. Wang, C. Fan, J. He, P. Ding, E. Liang, and Q. Xue, “Double Fano resonances due to interplay of electric and magnetic plasmon modes in planar plasmonic structure with high sensing sensitivity,” *Opt. Express*, vol. 21, no. 2, p. 2236, Jan. 2013, doi: 10.1364/OE.21.002236.

[40] J. B. Pendry, A. J. Holden, D. J. Robbins, and W. J. Stewart, “Magnetism from conductors and enhanced nonlinear phenomena,” *IEEE Trans. Microwave Theory Techn.*, vol. 47, no. 11, pp. 2075–2084, Nov. 1999, doi: 10.1109/22.798002.

[41] X. Long, M. Zhang, Z. Xie, M. Tang, and L. Li, “Sharp Fano resonance induced by all-dielectric asymmetric metasurface,” *Optics Communications*, vol. 459, p. 124942, Mar. 2020, doi: 10.1016/j.optcom.2019.124942.